LBNL-39196
UC-413
Preprint

ERNEST ORLANDO LAWRENCE
BERKELEY NATIONAL LABORATORY

Aspects of Reducibility and Thermal Scaling in Multifragmentation

R. Ghetti, L.G. Moretto, L. Phair,
K. Tso, and G.J. Wozniak
Nuclear Science Division

December 1996
Submitted to
Nuclear Physics A

LBNL-39196
UC-413

Aspects of reducibility and thermal scaling in multifragmentation

R. Ghetti[1], L. G. Moretto, L. Phair, K. Tso and G. J. Wozniak

Nuclear Science Division
Ernest Orlando Lawrence Berkeley National Laboratory
University of California, Berkeley, California 94720 USA

[1]Department of Physics
Lund University
Lund, Sweden

December 13, 1996

This work was supported in part by the Director, Office of Energy Research, Office of High Energy and Nuclear Physics, Division of High Energy Physics, of the U.S. Department of Energy under Contract No. DE-AC03-76SF00098.

Aspects of Reducibility and Thermal Scaling in Multifragmentation

R. Ghetti [1], L.G. Moretto, L. Phair, K. Tso, G.J. Wozniak

Nuclear Science Division, Lawrence Berkeley National Laboratory, Berkeley, CA 94720, USA

Abstract

Recent experimental evidence of binomial reducibility and thermal scaling in multifragmentation, has raised a number of physical and technical issues that need to be addressed. To this end, two simulations of multifragment decay have been implemented, a binomial simulation and a Poisson one. By means of the binomial simulation, the reducibility of the n-fold intermediate-mass-fragment multiplicity and charge distributions to the one-fragment emission values has been investigated. With both simulations, the effects of using the transverse energy as a measure of the system excitation energy have been evaluated. Possible experimental biases in the results have been evaluated as well.

1 Introduction

Multifragmentation has been the subject of intense debate during the last decade [1–3]. At low bombarding energy ($E/A \leq 20$ MeV), intermediate mass fragments (IMF: $3 \leq Z \leq 20$) are emitted with low probability by a well understood compound nucleus decay mechanism [4,5]. By increasing the bombarding energy, the binary signature of compound nucleus decay disappears, and the probability of multiple IMF emission rapidly increases [1]. At intermediate energies ($30 < E/A < 100$ MeV), the reaction mechanism governing the production of IMFs is not well characterized.

A hotly debated question regarding multifragmentation is whether the decay is driven by statistics [6–11] or dynamics [12–15]. Insight into this issue has been gained by analyzing intermediate energy heavy ion data in a particularly revealing way, inspired by α-induced fission studies [16]. In the fission case, the statistical nature of the rise of the fission probability P with the excitation energy E^*, was demonstrated by the presence of a linear dependence between $\ln(P)$ and $1/\sqrt{E^*}$ (Arrhenius plot). For the

[1] Present address: Department of Physics, Lund University, Sweden

multifragmentation case, the n-fold fragment emission probabilities P_n, defined as: $P_n = N(n)/\sum_{n=0}^{\infty} N(n)$, where $N(n)$ is the number of events with n IMFs, show the same characteristic energy dependence as low energy fission, pointing to their statistical origin. This was first demonstrated in a study of ^{197}Au + ^{27}Al,^{51}V,^{nat}Cu reactions at E/A = 60 MeV [17], and more recently in a methodic experimental investigation of ^{36}Ar + ^{197}Au reactions at beam energies of E/A = 80 and 110 MeV [18] and ^{129}Xe-induced reactions on several targets (^{nat}Cu, ^{89}Y, ^{165}Ho, ^{197}Au) at E/A = 40, 50 and 60 MeV [19].

In the studies of Refs. [18,19], the emission probabilities P_n were measured as a function of the total transverse kinetic energy E_t, which was used to estimate the excitation energy. E_t is defined as the sum of the kinetic energies E, weighted by the sine squared of the polar angle θ for all detected particles in an event:

$$E_t = \sum E_i \sin^2 \theta_i. \tag{1}$$

At all transverse energies, the probabilities P_n of emitting n fragments were found to rigorously obey the binomial distribution:

$$P_n = p^n (1-p)^{m-n} \frac{m!}{n!(m-n)!}, \tag{2}$$

with average IMF multiplicity $\langle n \rangle = pm$ and variance $\sigma^2 = pm(1-p)$. In the above expressions, m is the number of independent tries, and p the binomial probability of success. More specifically, p represents the elementary probability for single fragment emission, to which the probabilities for n-fragment emission P_n are *reducible*, through the binomial equation. An example of experimental excitation functions, together with their mean and variance, is presented in Figs. 1a,b.

The values of p and m can be extracted at each transverse energy from the experimental values of the mean and variance. In the work of Refs. [18,19], the Arrhenius plot $\ln(1/p)$ versus $1/\sqrt{E_t}$, was constructed for the extracted values of the elementary probability p, and was found to be remarkably linear for almost all systems studied [18,19]. An example is given in Fig. 1d.

Assuming proportionality between E_t and the excitation energy [18–23], the linearity of the Arrhenius plot implies that the one-fragment emission probability p has a *thermal* dependence with a Boltzmann form:

$$p \propto \exp(-B/T) \tag{3}$$

where $T \propto \sqrt{E_t}$ and B represents the average barrier for fragment emission.

Finally, the features of reducibility (Eq. (2)) and thermal scaling (Eq. (3)) of the fragment emission probabilities have been shown to extend consistently also to the charge distributions [21,24], and to the light charged particle angular correlations [22]

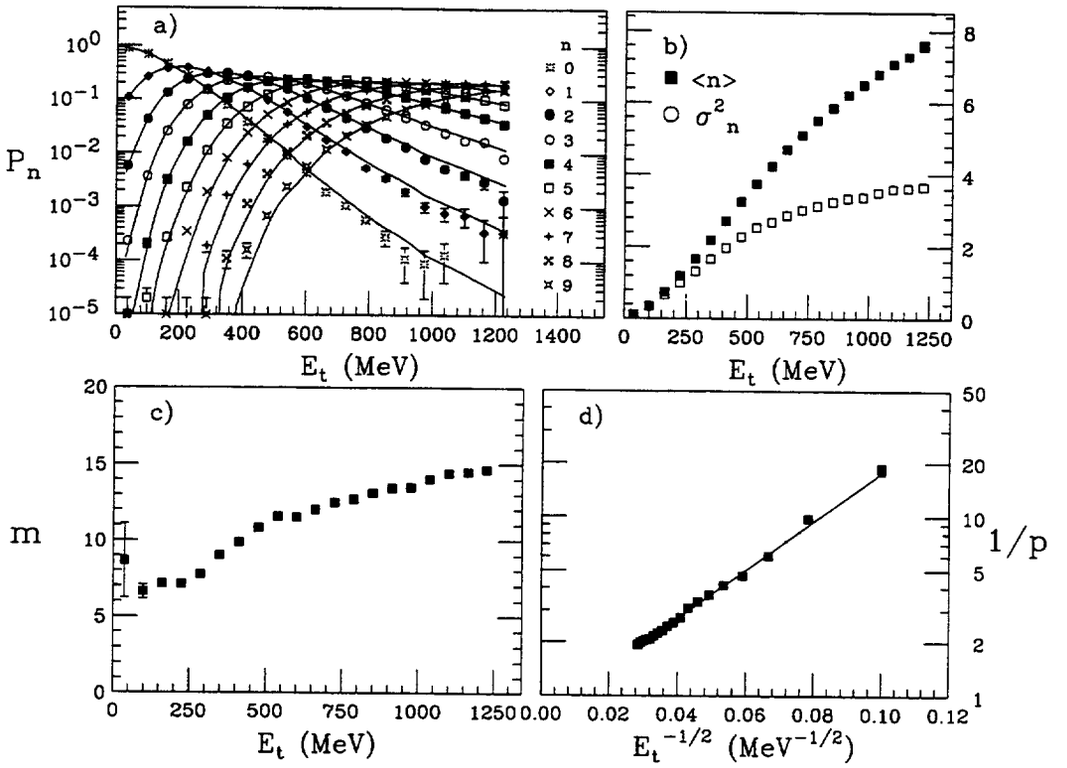

Fig. 1. Experimental data from the ^{129}Xe + ^{197}Au reaction at E/A = 50 MeV [19]. a) The experimental (symbols) and the calculated (solid lines) probabilities P_n of emitting n IMFs as a function of the transverse energy E_t. For number of fragments $n = 0 - 9$, P_n are calculated assuming a binomial distribution (Eq. (2)) with the values of p obtained from the linear fit shown in d) and the values of m shown in c). b) Mean (squares) and variance (circles) of the multiplicity distributions as a function of E_t. c) Values of m extracted from the mean and the variance (see Eqs. (8)), as a function of E_t. d) Values of $1/p$ extracted from the mean and the variance (see Eqs. (8)), as a function of $1/\sqrt{E_t}$. Solid line: linear fit.

associated with multifragmentation. An extensive discussion of these results can be found in [23].

The remarkable description of the IMF emission probabilities by the binomial distribution, gives significant insight into the nature of multifragmentation, since reducibility of the n-fold emission probabilities means that all the physics controlling P_n is contained in the binomial parameters p and m. This, in turn, implies that multifragmentation itself is empirically reducible to a combination of nearly independent fragment emissions. One possible physical interpretation is sequential decay with constant probability p. In this description, the number of trials in the binomial distribution, m, can be interpreted as the number of chances the system has to emit a fragment. Alternatively, one can picture the multifragment decay process as a chain of m links with probability p that any of the links is broken [18], or as simultaneous statistical decay as in Ref. [25].

The experimental observations of reducibility and thermal scaling, along with the

insight they provide into the nature of the multifragmentation process, raise several issues directly related to binomiality, as well as a number of technical questions connected to the experiments. This has prompted us to implement two schematic Monte Carlo simulations of multifragment decay, a binomial simulation and a Poisson one. Multifragment events, simulated with different input conditions and processed in the same fashion as the experimental data, have been used to clarify these issues, as will be discussed in detail in the following sections.

The paper is organized as follows: Sec. 2 describes the binomial event generator and presents selected results on physical features related to reducibility and thermal scaling. The effects of using the transverse energy as a measure of the system excitation energy are evaluated by means of a Poisson simulation in Sec. 3. Technical problems, such as efficiency effects on the binomial distributions and effects of the experimental filter, are discussed in Sec. 4. A summary of the results can be found in Sec. 5.

2 Binomial Simulation

2.1 Monte Carlo Event Generator

A Monte Carlo algorithm has been implemented to generate multifragment events, characterized by reducibility and thermal scaling in the fragment multiplicity distributions and in the charge distributions, in qualitative agreement with the experimental data. To this end, a source of mass A_0, charge Z_0 and excitation energy E^* deexcites by emitting a fixed number (m_o) of particles. The decay chain is implemented through m_o steps, that can be thought of as either time-like or space-like. The result of each step is either the emission of one neutron or the emission of an *inert* charged particle (Z = 1 - 20). Neutrons participate in all m_o steps, while particles of charge Z participate in only $m_Z = m_o/Z$ steps. By choosing $m_Z = m_o/Z$, we are consistent with the experimental observation that the value of m decreases with increasing $Z_{\rm th}$, the lower charge in the IMF definition, roughly scaling as $m \cdot Z_{\rm th}$ [23,26]. The $m \cdot Z_{\rm th}$ scaling will be discussed in Sec. 2.3.2.

The Monte Carlo algorithm is implemented in the following way. For the i^{th} step, the maximum participating Z is $Z_{max} = m_o/i$, and the emission probabilities are:

$$p_Z(i) = C_N(Z_{max}) \exp(\frac{-b \cdot Z}{T}), \quad Z = 1, Z_{max}(i), \quad i = 1, m_o. \tag{4}$$

In Eq. (4), the nuclear temperature T is parametrized as in the Fermi gas model: $T = \sqrt{E^*/a}$, ($a = A_0/8.5$). The fragment emission barrier $B_Z = (b \cdot Z)$ contains a Z dependence suggested by the Coulomb interaction, and is kept constant throughout

the decay process. The probability for neutron emission is taken as:

$$p_0(i) = C_N(Z_{max}), \quad i = 1, m_o, \tag{5}$$

and the normalization constant $C_N(Z_{max})$ is chosen so that:

$$\sum_{Z=0}^{Z_{max}} p_Z(i) = 1. \tag{6}$$

A fragment of charge Z is assigned a mass number A determined from the parametrization $A = 2.08Z + 0.0029Z^2$ [27]. Charge and mass are then conserved in the simulation. If the fragment extracted in the i^{th} step is larger than the residual source, the i^{th} emission is prohibited, thus effectively reducing the number of emissions with respect to the input parameter m_o.

The simulations are performed as a function of the excitation energy, upon which the decay process depends through the fragment emission probabilities p_Z (Eq. (4)). As to the number of binomial throws m_o, we have performed calculations with both a constant value of m_o and with m_o linearly increasing with E^* (see Sec. 2.3.2).

In order to evaluate the transverse energy of the simulated events, each fragment is assigned a finite radius appropriate to its size, according to the empirical parametrization: $r = 1.128A^{1/3}(1 - 0.786A^{-2/3})$ [28]. The fragments are then isotropically distributed in a sphere of dilute nuclear matter (half normal density) and given an initial momentum. Under the assumption of thermal equilibrium, the initial momenta are determined from an equal sharing of the available excitation energy among all emitted particles (including neutrons and light charged particles). The trajectories of the source and all emitted fragments, under their mutual Coulomb interaction, are calculated classically. Angular momentum effects are neglected.

Events, characterized by excitation energy E^*, transverse energy E_t, total multiplicity m_o and single particle observables (mass and atomic number, kinetic energy, polar and azimuthal angles), are produced following the above prescription and analyzed.

2.2 Analysis of the Simulated Events

Simulations for sources of ^{197}Au, ^{129}Xe and ^{64}Cu have been performed to compare with experimental results from the ^{36}Ar + ^{197}Au [18] and ^{129}Xe-induced [19] reactions. The simulated events have been analyzed using the same procedures utilized for the experimental data analysis. The conventional IMF definition $3 \leq Z_{\rm IMF} \leq 20$ (i.e. $Z_{\rm th} = 3$) is used, except where specified otherwise. At each value of E^*, the binomial parameters p and m are extracted from the binomial relationships:

$$\langle n \rangle = pm, \qquad \sigma^2 = pm(1-p) \tag{7}$$

which can be rewritten as:

$$p = 1 - \frac{\sigma^2}{\langle n \rangle}, \qquad m = \frac{\langle n \rangle^2}{\langle n \rangle - \sigma^2} \tag{8}$$

where $\langle n \rangle$ and σ^2 are the mean and the variance of the fragment multiplicities. The recovered parameters p and m, when introduced in Eq. (2), provide an accurate fit of the n-fold IMF emission probabilities. As an example, Fig. 2 shows the calculated multifragment emission probabilities P_n from the decay of a ^{197}Au source (Fig. 2a) along with the values of $1/p$ (Fig. 2d) and m (Fig. 2c) extracted from the mean and variance of the multiplicity distributions (Fig. 2b) at each excitation energy. The solid lines in Fig. 2a represent a binomial fit to the excitation functions, calculated from Eq. (2) with the values of m and p extracted according to Eq. (8). The binomial fit is in excellent agreement with the multiplicity distributions, except for a few points at the lowest values of the excitation energy. This is due to the fact that, in the limit of very low temperature, the n-fragment probability distributions approach the Poissonian limit, as indicated by the equal values of the mean and variance (Fig. 2b).

2.3 Selected Results

In this section we present results from binomial simulations which address relevant issues connected to binomial reducibility and thermal scaling.

2.3.1 The Binomial Parameter p. Arrhenius Plots. Barrier Extraction

As pointed out in Sec. 1, a linear Arrhenius plot $\ln(1/p)$ versus $1/\sqrt{E}$ implies a thermal behavior of p, i. e. $p \propto \exp(-B/T)$, and information on the effective emission barrier B can be extracted from the slope of the plot. This procedure for barrier determination relies on the assumption that, when a hierarchy of different barriers is present to govern the decay (Eq. (4)), the average p is dominated by the lightest fragment with the lowest barrier [19,23].

With our binomial simulation we can estimate the reliability of this approximation and the systematic error associated with the barrier extracted through this procedure. We start by simulating the binomial decay of an excited source and proceed by extracting the "observed" binomial probability p from the mean and variance of the calculated IMF multiplicity distributions (Eq. (8)). We then plot the natural logarithm of $1/p$ as a function of $1/\sqrt{E^*}$. Since the resulting Arrhenius plot obeys

$$1/p = e^{-B_{\rm obs}/T}, \tag{9}$$

the "observed" fragment emission barrier $B_{\rm obs} = b_{\rm obs} \cdot Z_{\rm th}$ can be readily extracted and compared with the simulation input value b.

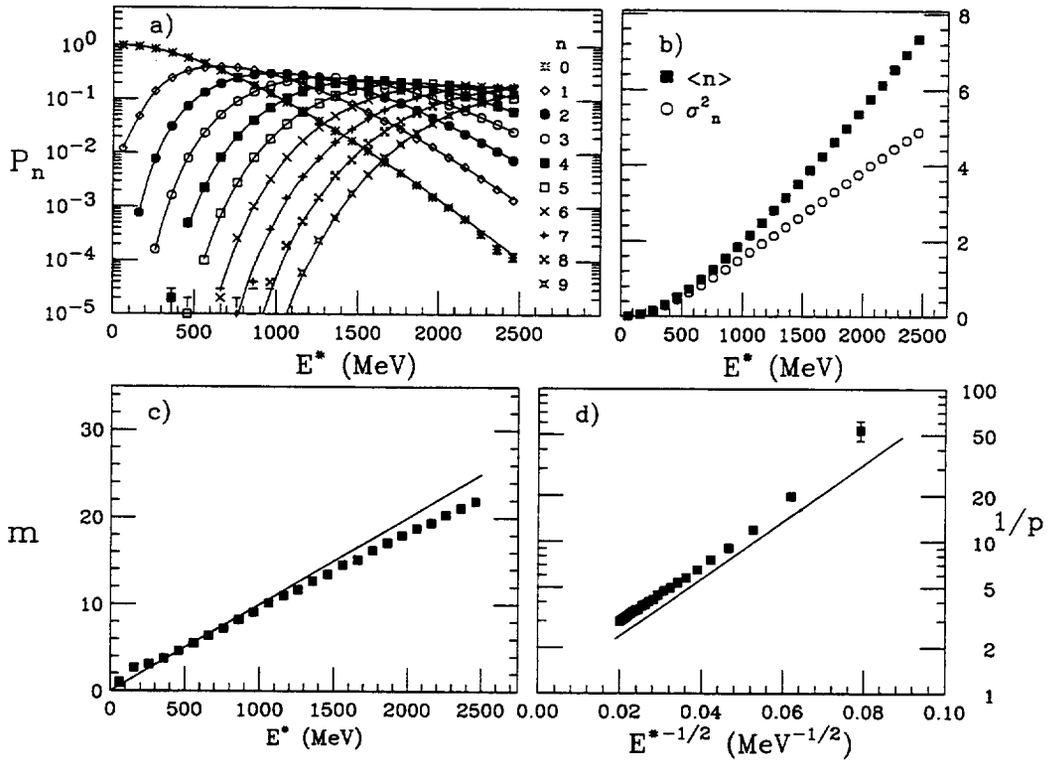

Fig. 2. Binomial decay of a ^{197}Au source with excitation energies in the range of 100 to 2500 MeV and binomial parameters $m_o(E^*) = 0.03 \cdot E^*$, $B_Z = (3 \cdot Z)$ MeV. a) The simulated (symbols) and the recalculated (solid lines) probabilities P_n of emitting n IMFs as a function of the excitation energy E^*. For number of fragments $n = 0-9$, P_n are calculated assuming a binomial distribution with the values of p shown in d) and the values of m shown in c). b) Mean (squares) and variance (circles) of the multiplicity distributions as a function of E^*. c) Values of m extracted from the mean and the variance, as a function of E^*. Solid line: simulation input m_o/Z, $Z = 3$. d) Values of $1/p$ extracted from the mean and the variance, as a function of $1/\sqrt{E^*}$. Solid line: simulation input $1/p$ for Z=3.

Fig. 3a presents Arrhenius plots from the decay of a ^{197}Au source, with initial excitation energies in the range of 100 to 2500 MeV and binomial input parameters $B_Z = (3 \cdot Z)$ MeV and $m_o(E^*) = 0.03 \cdot E^*$. The Arrhenius plots are constructed for values of Z_{th} equal to 3, 5 and 7, and are seen to become progressively steeper for increasing Z_{th}. The barriers extracted from the slopes of the Arrhenius plots, are in good agreement with the input barriers, from which they differ by less than 5%.

These simulations strongly support the experimental evidence presented in Refs. [19,29], where the dependence of the barrier on Z has been explored by constructing Arrhenius plots for increasing values of the lower threshold Z_{th} in the IMF definition. Fig. 3b shows an example of experimental Arrhenius plots from ^{129}Xe + ^{197}Au reactions at E/A = 60 MeV. The slope of the plots is found to increase with Z_{th}, in qualitative agreement with the simulation results. Since the decay barrier, dominated by the Coulomb interaction, is proportional to the atomic number of the emitted fragment, the observed Z_{th} dependence suggests that the decay is truly dominated by

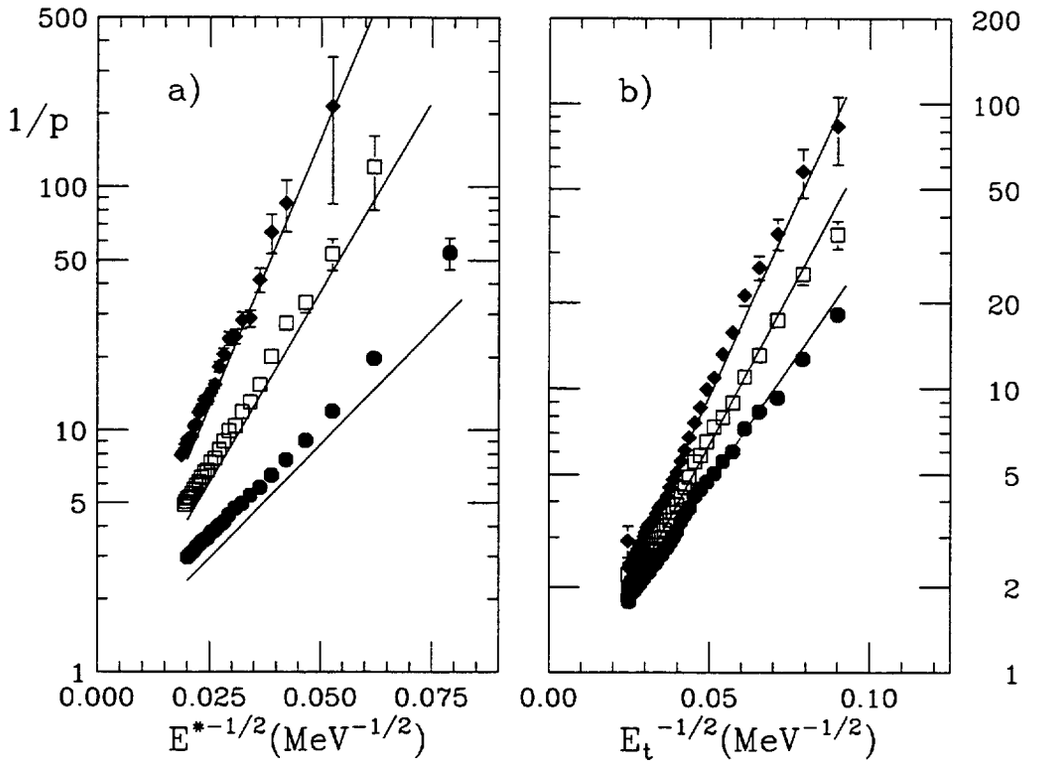

Fig. 3. a) From the simulated binomial decay of a ^{197}Au source with excitation energies and binomial parameters as in Fig. 2: E^*-Arrhenius plots from the analysis of the mean and variance of the IMF excitation functions (Fig. 2b), for different values of $Z_{\rm th}$ in the IMF definition (circles: $Z_{\rm th}$=3, squares: $Z_{\rm th}$=5, diamonds: $Z_{\rm th}$=7). Solid lines: simulation input barriers for $Z = 3, 5, 7$ fragments. b) From the experimental ^{129}Xe + ^{197}Au reaction at E/A = 60 MeV: E_t-Arrhenius plots from the analysis of the mean and variance of the IMF excitation functions, for different values of $Z_{\rm th}$ in the IMF definition (circles: $Z_{\rm th}$=3, squares: $Z_{\rm th}$=5, diamonds: $Z_{\rm th}$=7). Solid lines: linear fits.

the lightest fragment. Moreover, the sensitivity of the slopes of the Arrhenius plots to $Z_{\rm th}$, consistent with the Z dependence of the emission barrier B_Z, is a powerful signal for the physical meaning of p.

2.3.2 The Binomial Parameter m

From the mean and variance of the IMF multiplicity distributions produced by the decay of a ^{197}Au source, the values of m have been extracted according to Eq. (8), and are shown in Fig. 4a for values of $Z_{\rm th}$ equal to 3, 5 and 7. The extracted values of m agree well with the simulation input values m_o/Z, represented by the straight lines. For comparison Figs. 4b,c show experimental values of m, as a function of E_t, for the reaction ^{129}Xe + ^{197}Au at bombarding energies of E/A= 40 MeV (Fig. 4b) and 60 MeV (Fig. 4c). The different symbols represent values of m extracted with different values of $Z_{\rm th}$ (3, 5 and 7).

The parameter m that appears in the binomial picture of multifragment decay, has

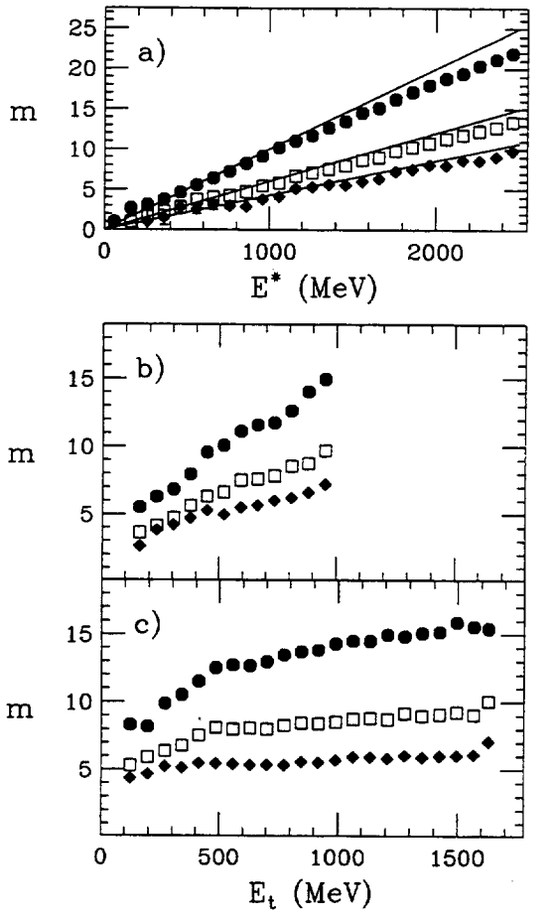

Fig. 4. a) From the simulated binomial decay of a ^{197}Au source with excitation energies and binomial parameters as in Fig. 2: values of m extracted from the analysis of the mean and variance of the IMF excitation functions (Fig. 2b), for different values of $Z_{\rm th}$ in the IMF definition (circles: $Z_{\rm th}$=3, squares: $Z_{\rm th}$=5, diamonds: $Z_{\rm th}$=7). Solid lines: simulation input values of $m_{\rm o}/Z$ for $Z = 3, 5, 7$ fragments. b,c) From the experimental ^{129}Xe + ^{197}Au reaction at E/A = 40 MeV (b) and 60 MeV (c), values of m as a function of E_t, for different values of $Z_{\rm th}$ in the IMF definition (circles: $Z_{\rm th}$=3, squares: $Z_{\rm th}$=5, diamonds: $Z_{\rm th}$=7).

a problematic interpretation. Our understanding is that it may be associated with the dynamics of the decay process. In a sequential scenario, the quantity m defines a time window, possibly determined by the dynamics, during which fragment emission is allowed. Simulations performed with the "Emission Expansion Source" model [30], for example, show that the value of m, and its dependence on the available excitation energy, are very sensitive to the initial expansion rate [31]. In a space-like interpretation instead, m could be connected to the finiteness of the source size. Speculative discussion on this subject can be found in [23].

When implementing the algorithm used for the binomial decay simulations, we have tried different and somewhat arbitrary choices for the input value $m_{\rm o}$. While some of the experimental data seem to suggest a nearly linear dependence of m on the transverse energy (see for example Figs. 1c, 4b), a value of m constant with E^* appears

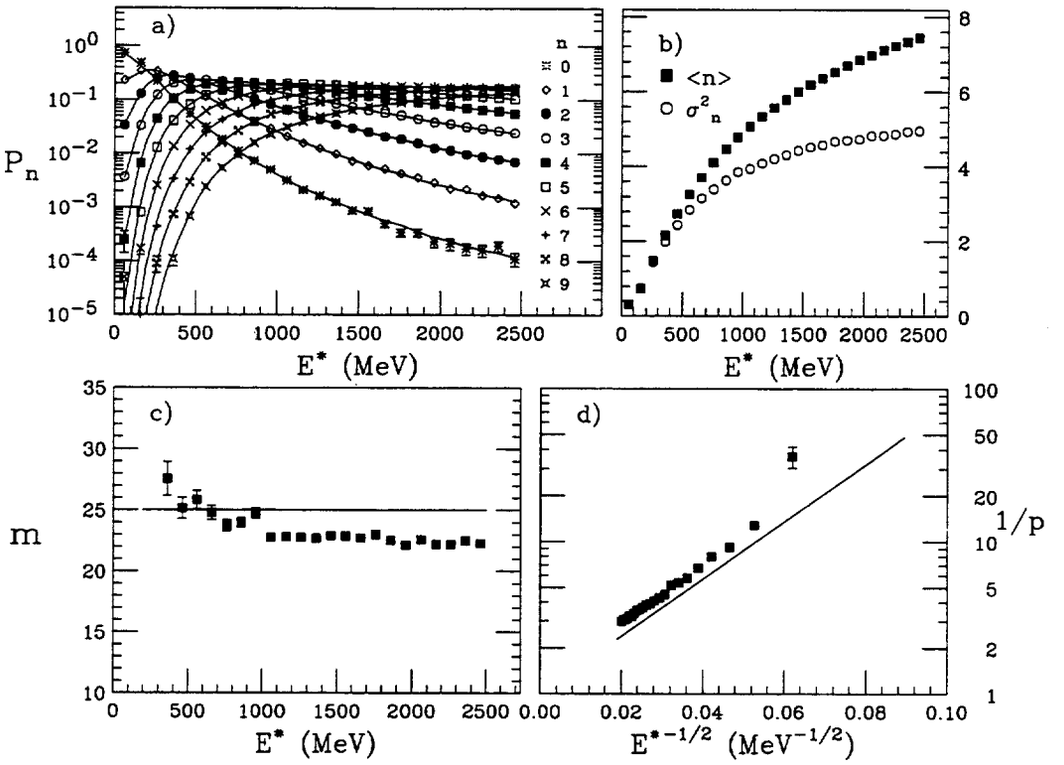

Fig. 5. Binomial decay of a ^{197}Au source with excitation energies in the range of 100 to 2500 MeV and binomial parameters $m_o = 75$, $B_Z = (3 \cdot Z)$ MeV. a) The simulated (symbols) and the recalculated (solid lines) probabilities P_n of emitting n IMFs as a function of the excitation energy E^*. For number of fragments $n = 0 - 9$, P_n are calculated assuming a binomial distribution with the values of p shown in d) and the values of m shown in c). b) Mean (squares) and variance (circles) of the multiplicity distributions as a function of E^*. c) Values of m extracted from the mean and the variance, as a function of E^*. Solid line: simulation input m_o/Z, $Z = 3$. d) Values of $1/p$ extracted from the mean and the variance, as a function of $1/\sqrt{E^*}$. Solid line: simulation input $1/p$ for Z=3.

better justified from a physical point of view, since, in our simulation, the excitation energy dependence of the decay process is already taken into account through the fragment emission probabilities p_Z (Eq. (4)). Fig. 5 is analogous to Fig. 2, but now the input m_o has been fixed to m_o=75 for all excitation energies. The results presented in Fig. 5 and Fig. 2 are somewhat similar, and a comparison with the experimental data does not resolve the issue.

Another arbitrary choice that we have made in our code, is to impose the condition that a particle of charge Z can only participate in m_Z=m_o/Z out of m_o trials. As we have already mentioned in Sec. 2.1, this is motivated by the experimental observation of the scaling $m \cdot Z_{th} \approx$ constant, shown in Figs. 6a,b for the ^{129}Xe + ^{197}Au reaction at E/A= 40 MeV and 60 MeV. This experimental scaling seems to indicate a space-like interpretation of multifragment decay, with a source of finite charge Z_o breaking into no more than $m = Z_o/Z$ fragments of charge Z.

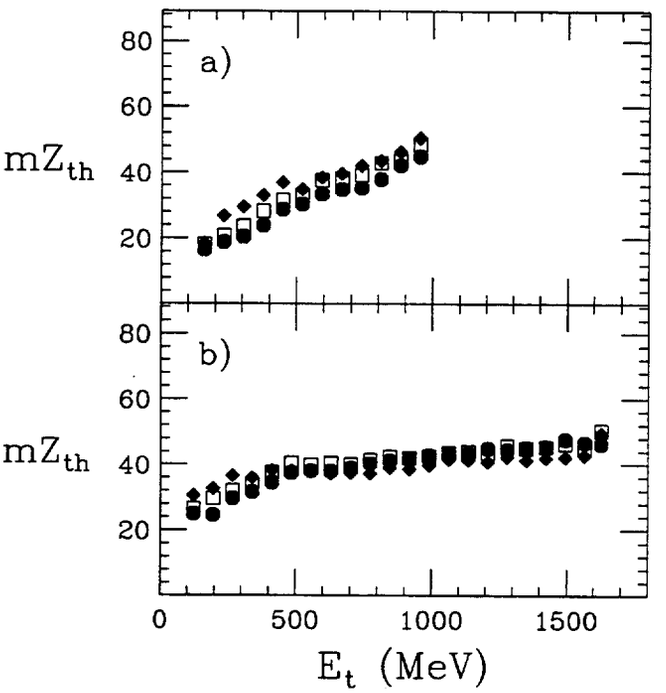

Fig. 6. From the experimental ^{129}Xe + ^{197}Au reaction at E/A = 40 MeV (a) and 60 MeV (b), values of values of $mZ_{\rm th}$ as a function of E_t (circles: $Z_{\rm th}$=3, squares: $Z_{\rm th}$=5, diamonds: $Z_{\rm th}$=7).

A clear limitation of our simulation is that the above scaling is introduced *ad hoc* and does not originate from the finite size of the decaying source. We have proceeded in this way because, if we allow fragments of all sizes to be emitted in all $m_{\rm o}$ trials, our algorithm loses stability: the IMF multiplicities vary wildly event-by-event, and the IMF excitation functions are no longer binomial.

2.3.3 Binomial Distributions and Source Residues

The features of reducibility and thermal scaling of multifragment decay are experimentally inferred from the binomiality of the IMF excitation functions [18,19]. Consequently, this kind of experimental data analysis relies on the precision of the binomial counting scheme. It is reasonable to expect that the detection of residual fragments, bearing genetic relationship to either the target or the projectile, may spoil the binomiality of the distributions. Since, experimentally, it is not always possible to distinguish between true reaction products and residue-like spectators, it is important to investigate the effects on binomial reducibility, of residue-like spectators misidentified as true reaction products.

The results from the simulations presented so far, have been obtained by neglecting the source residue (that in the ^{197}Au case, for example, is always present at the end of the decay chain for $E^* \leq 2500$ MeV). The analysis has therefore been repeated, counting the source residue as one IMF, if the residue's atomic number falls within

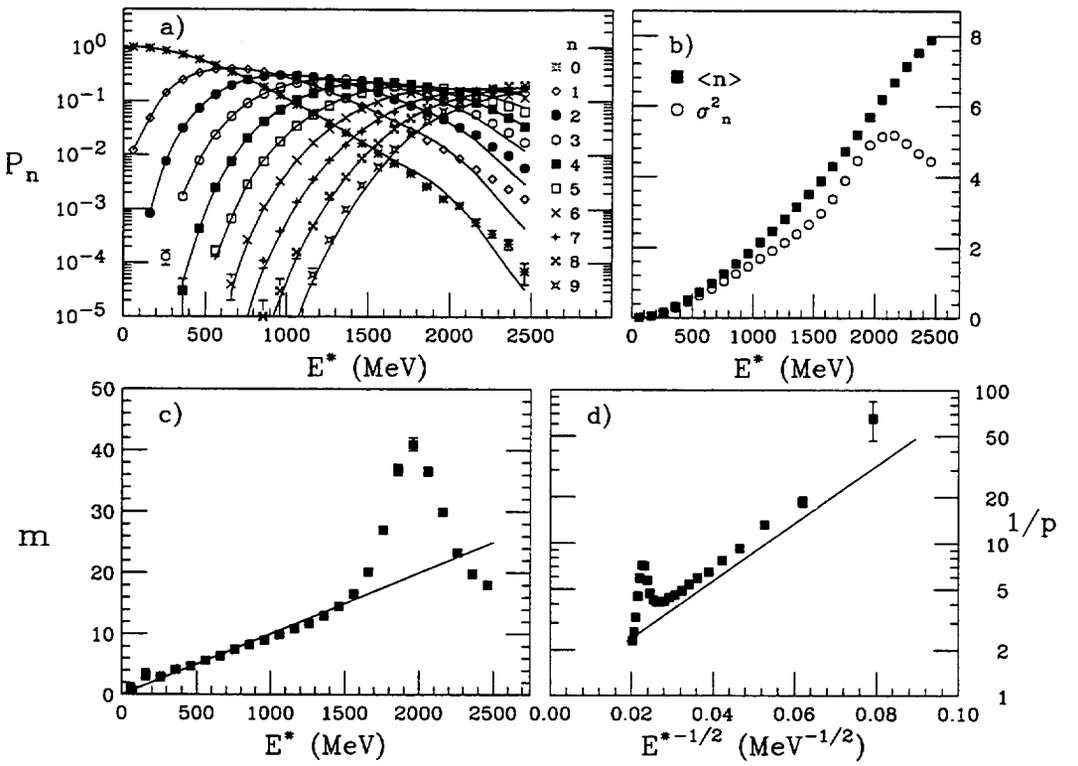

Fig. 7. Binomial decay of a ^{197}Au source with excitation energies and binomial parameters as in Fig. 2. The source residue is now included in the analysis. a) The simulated (symbols) and the recalculated (solid lines) probabilities P_n of emitting n IMFs as a function of the excitation energy E^*. For number of fragments $n = 0 - 9$, P_n are calculated assuming a binomial distribution with the values of p shown in d) and the values of m shown in c). b) Mean (squares) and variance (circles) of the multiplicity distributions as a function of E^*. c) Values of m extracted from the mean and the variance, as a function of E^*. Solid line: simulation input m_o/Z, $Z = 3$. d) Values of $1/p$ extracted from the mean and the variance, as a function of $1/\sqrt{E^*}$. Solid line: simulation input $1/p$ for Z=3.

the IMF definition $3 \leq Z_{\rm IMF} \leq 20$. The results are summarized in Fig. 7.

Inclusion of the residue in the binomial counting scheme, produces a larger dispersion of the IMF multiplicity distributions (Fig. 7b) compared to the purely binomial case (Fig. 2b). Consequently a pronounced "bump" appears in the Arrhenius plot (Fig. 7d) as well as in the extracted values of m (Fig. 7c). The binomial fit of the IMF probability distributions, obtained with the extracted values of m and p, is however still rather accurate, as can be seen in Fig. 7a.

These simulations show that the analysis of reducibility and thermal scaling in the experimental data is affected by detection of residue-like spectators. However, favorable conditions can be devised to prevent this from happening. In the laboratory, high energy projectile-like residues can be kinematically focused beyond the geometric acceptance of the detection device by performing reverse kinematics reactions. Low energy target-like spectators can be stopped by setting sufficiently high detec-

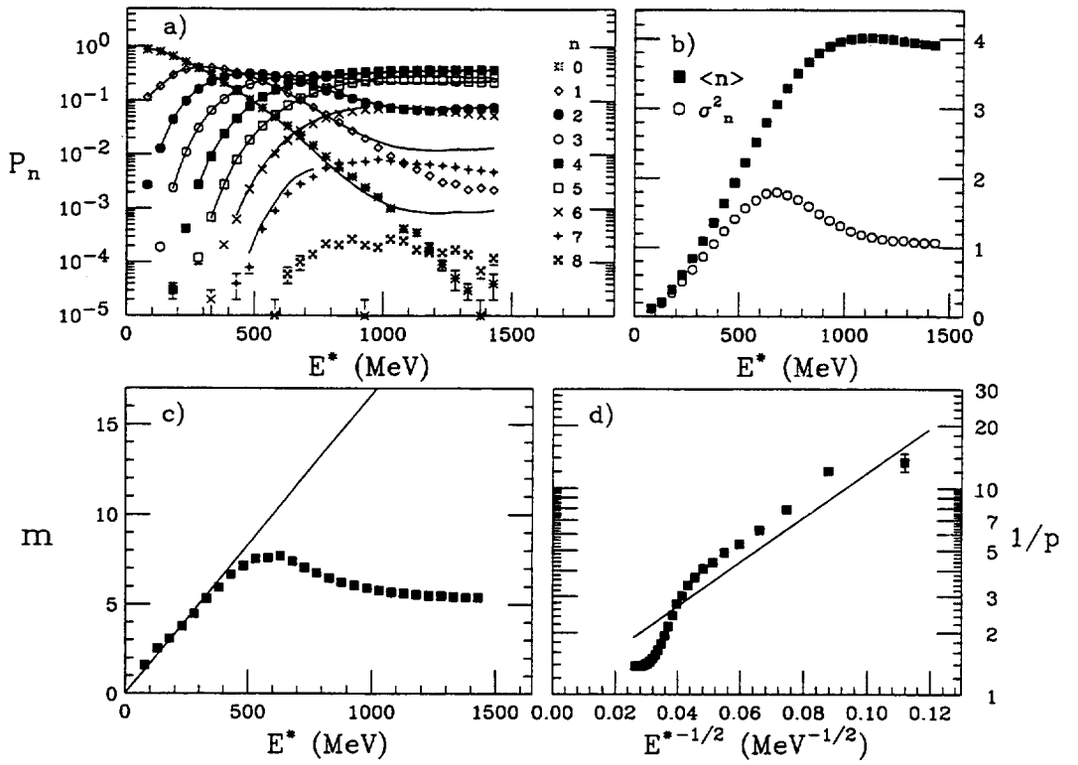

Fig. 8. Binomial decay of a ^{64}Cu source with excitation energies in the range of 100 to 1500 MeV and binomial parameters $m_o(E^*) = 0.05 \cdot E^*$, $B_Z = (3 \cdot Z)$ MeV. a) The simulated (symbols) and the recalculated (solid lines) probabilities P_n of emitting n IMFs as a function of the excitation energy E^*. For number of fragments $n = 0 - 8$, P_n are calculated assuming a binomial distribution with the values of p shown in d) and the values of m shown in c). b) Mean (squares) and variance (circles) of the multiplicity distributions as a function of E^*. c) Values of m (squares) extracted from the mean and the variance, as a function of E^*. Solid line: simulation input m_o/Z, $Z = 3$. d) Values of $1/p$ (squares) extracted from the mean and the variance, as a function of $1/\sqrt{E^*}$. Solid line: simulation input $1/p$ for Z=3.

tion energy thresholds. On the software level, restrictions of the IMF definition, as well as event-by-event exclusion of the largest fragment from the binomial counting scheme, can help avoid contamination from spectator-like residues.

2.3.4 Binomial Distributions and Small Size Effects

Another issue that we want to address is whether reducibility and thermal scaling are sensitive to the physical constraints of charge and mass conservation, that come into play when the source of fragment emission is small.

To this end, we have simulated the decay of a small ^{64}Cu source. A striking feature characterizing the ^{64}Cu results, presented in Fig. 8 and obtained without counting the source residues, is that the extracted values of m strongly deviate from the linear input and saturate at high values of E^* (Fig. 8c). This saturation reflects the way that charge and mass are conserved in the simulation. At large excitation energies, it sometimes

happens that the fragment extracted in the i^{th} step is larger than the residual source. In this case the i^{th} emission is inhibited, leading to an effectively reduced number of emissions with respect to the input parameter m_o. For the particular ^{64}Cu source simulation of Fig. 8, this happens at values of $E^* \geq$500 MeV, in correspondence to the region where the deviation of m from the input values appears. Also the behavior of the Arrhenius plot is affected by the conservation constraints. Fig. 8d shows that the plot loses its linearity in the high excitation energy region ($E^* > 500$ MeV).

In conclusion, the simulation results suggest that the experimental analysis of binomial reducibility and thermal scaling may be sensitive to small size effects. This will be discussed further in Sec. 2.3.6.

2.3.5 Binomial Distributions and Multiple Sources

Multifragmentation studies have revealed that often several sources are responsible for IMF emission. For example, investigation of the invariant fragment velocity plots in Xe-induced reactions, has shown that for peripheral collisions (i.e. at low values of E_t) one can clearly identify target-like, projectile-like and mid-rapidity or neck source [32–37]. Unexpectedly, the work presented in Ref. [19] shows that binomial reducibility and thermal scaling continue to hold even in the low E_t region. It is therefore important to study whether multiple sources of fragments are consistent with binomiality, and what is the meaning of a linear Arrhenius plot when multiple sources are present.

A linear Arrhenius plot does not exclude the presence of multiple sources. It is obvious that the decays of two binomial sources, with the same elementary probability p, are equivalent to the decay of one source with the same probability p and number of trials m equal to the sum of the number of trials m_1, m_2 of the two sources. This is the only case for which the sum of two binomial distributions gives an exact binomial distribution. However, the excitation functions obtained from two sources with different elementary probabilities can be approximated by a binomial distribution dominated by the source with the larger emission probability.

The distributions produced by two sources with binomial parameters (p_1, m_1) and (p_2, m_2) appear as one single distribution with mean and variance:

$$\langle n \rangle_{\rm obs} = p_1 m_1 + p_2 m_2 = p_{\rm obs} m_{\rm obs} \tag{10}$$

$$\sigma^2_{\rm obs} = p_1 m_1 (1 - p_1) + p_2 m_2 (1 - p_2) = p_{\rm obs} m_{\rm obs} (1 - p_{\rm obs}) \tag{11}$$

and can therefore be interpreted as originating from one source with binomial parameters:

$$p_{\rm obs} = \frac{m_1 p_1^2 + m_2 p_2^2}{m_1 p_1 + m_2 p_2}, \qquad m_{\rm obs} = \frac{(m_1 p_1 + m_2 p_2)^2}{m_1 p_1^2 + m_2 p_2^2}. \tag{12}$$

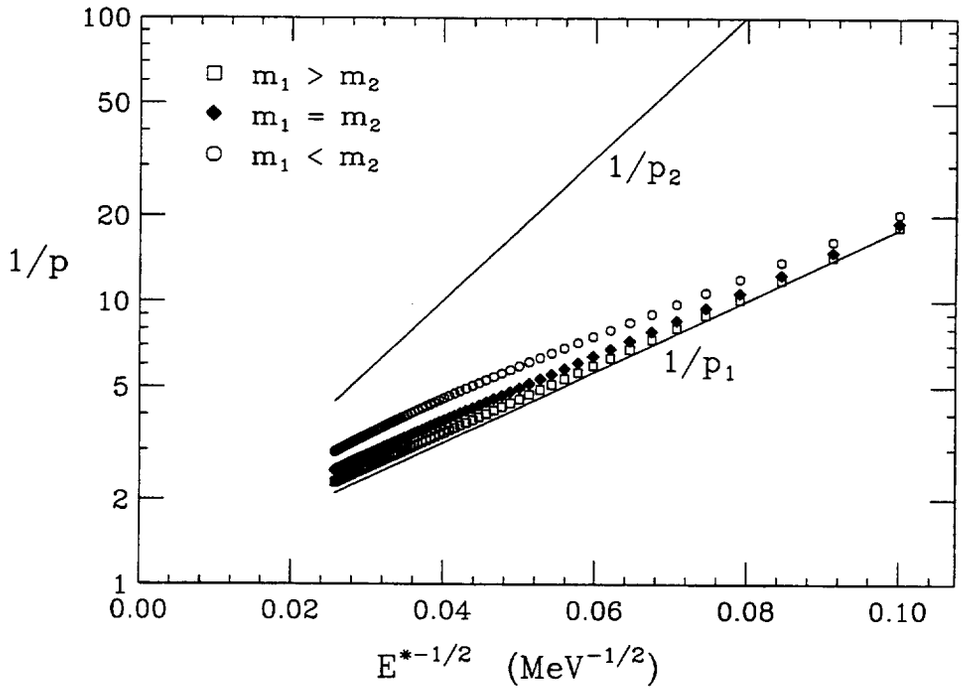

Fig. 9. Arrhenius plot from the binomial decay of two sources. Solid lines: $1/p$ corresponding to input values $B_1 = (3 \cdot Z)$ MeV, $B_2 = (4 \cdot Z)$ MeV. Symbols: Diamonds: $1/p_{\rm obs}$ for input $m_1 = m_2 = 20$. Squares: $1/p_{\rm obs}$ for input $m_1 = 40$, $m_2 = 20$. Circles: $1/p_{\rm obs}$ for input $m_1 = 20$, $m_2 = 40$.

In such a situation the Arrhenius plot is a nearly straight line and the barrier extracted from its slope is a good approximation to the true barrier of the dominant source, i.e. of the source with lower barrier (higher p) and/or higher m. The first relationship of Eqs. (12) is plotted in Fig. 9 (symbols) for combinations of two sources with various binomial input parameters. When one source dominates, reducing the excitation functions to the binomial distribution and extracting p and m, is still a suitable procedure to characterize the dominant source.

2.3.6 Reducibility of Charge Distributions

Reducibility and thermal scaling of the integrated fragment emission probabilities P_n observed in Refs. [18,19], raise the question of whether the charge distributions $P_n(Z)$ associated with multifragmentation are also reducible and scalable. The simplest condition required for the charge distributions to satisfy reducibility is that they are independent of the fragment multiplicity n, namely: $P_1(Z) = P_n(Z) = P_{\rm singles}(Z) = p(Z)$ [21]. However, experimental analysis of ^{36}Ar + ^{197}Au at E/A= 80 and 110 MeV, ^{129}Xe + ^{197}Au at E/A= 50 and 60 MeV, [21,38], ^{129}Xe + (^{nat}Cu, ^{197}Au) at $E/A = 30$ MeV [24] reactions, has revealed a weak residual systematic dependence of the charge distributions on the fragment multiplicity n. The n-fold charge distributions $P_n(Z)$

are in fact reducible to the corresponding 1-fold distribution through the scaling law:

$$P_n(Z) \propto \exp\left(-B_Z/T - ncZ\right) \tag{13}$$

where B_Z is the barrier for the emission of a fragment with charge Z, T is the temperature (assumed proportional to $\sqrt{E_t}$) and c is an empirical quantity characterizing the dependence of the charge distributions on the number of intermediate mass fragments n.

The reducibility of the n-fold event charge distributions to the 1-fold distribution through Eq. (13), demonstrates the near independence of individual fragment emission, with a limiting constraint manifested through the factor $\exp(-ncZ)$. Eq. (13) shows also that the thermal features observed for the n-fragment emission probability, and in particular the Boltzmann dependence of the elementary probability p, extend consistently to the charge distributions, strengthening the hypothesis of phase space dominance in multifragmentation [21,24].

In the binomial decay scenario, Eq. (13) is closely obeyed. The n-fold charge distributions manifest a thermal behavior: $P_n(Z) \propto \exp(-\alpha_n Z), \alpha_n \propto 1/T$, but do not meet the n-independence condition of extreme reducibility ($\alpha_1 = \alpha_2 = ... = \alpha_n = \alpha$), since a residual dependence of the form $\exp(-ncZ)$ appears.

The values of the quantity c are shown in Fig. 10, from the simulated decay of a ^{129}Xe source and a ^{64}Cu source. At each excitation energy, the value of c has been extracted from a linear fit to the logarithm of the ratio: $P_n(Z)/P_{n+1}(Z) = \exp(cZ)$, and a weighted average over all IMF multiplicities n. Fig. 10 shows that the quantity c starts with values near zero at low E^*, increases, and finally reaches a saturation value at high E^*. This behavior is similar to the behavior of the experimental quantity c with E_t [38]. One example from the ^{129}Xe + ^{197}Au reaction at E/A = 50 and 60 MeV, is shown in Fig. 11a for comparison.

The $c = 0$ region in the simulation, corresponds to emission from a source that survives as a charge conserving residue. Since each fragment does not know how many other fragments will follow it, the resulting charge distribution cannot reflect charge conservation under the constraint of n fragments. In such a scenario, charge conservation affects the distribution minimally. A large residue serves as a reservoir of mass, charge and excitation energy, weakening the charge correlations between fragments and thereby reducing c.

The transition region, where c increases with excitation energy, corresponds to the presence of a source residue whose dimensions are within the IMF definition. In the simulation, this is the moment when the small source size effects set in, since heavy IMF decay channels are effectively inhibited in order to conserve charge and mass. Finally, the $c > 0$ saturated region at high E^* indicates complete vaporization of the source in the simulation.

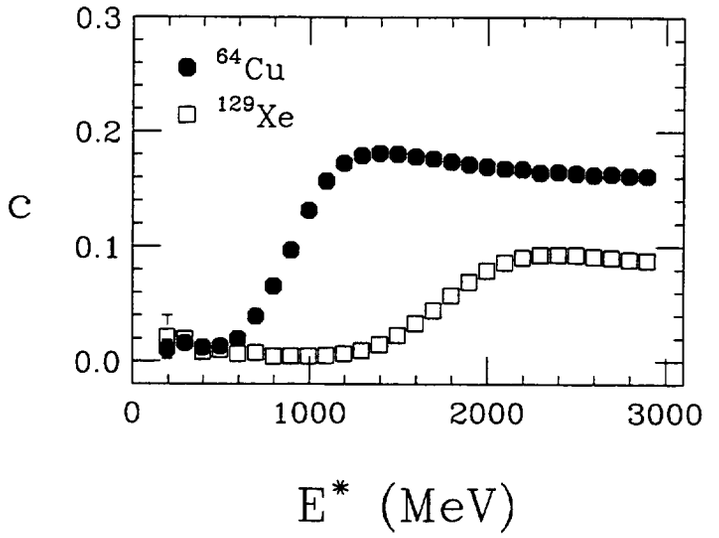

Fig. 10. From the binomial decay of a ^{129}Xe source (squares) and a ^{64}Cu source (circles) with excitation energies in the range of 100 to 3000 MeV and binomial parameters $m_o(E^*) = 0.05 \cdot E^*$, $B_Z = (3 \cdot Z)$ MeV: values of the quantity c, from the dependence of the IMF charge distributions on the fold number n, plotted as a function of the excitation energy.

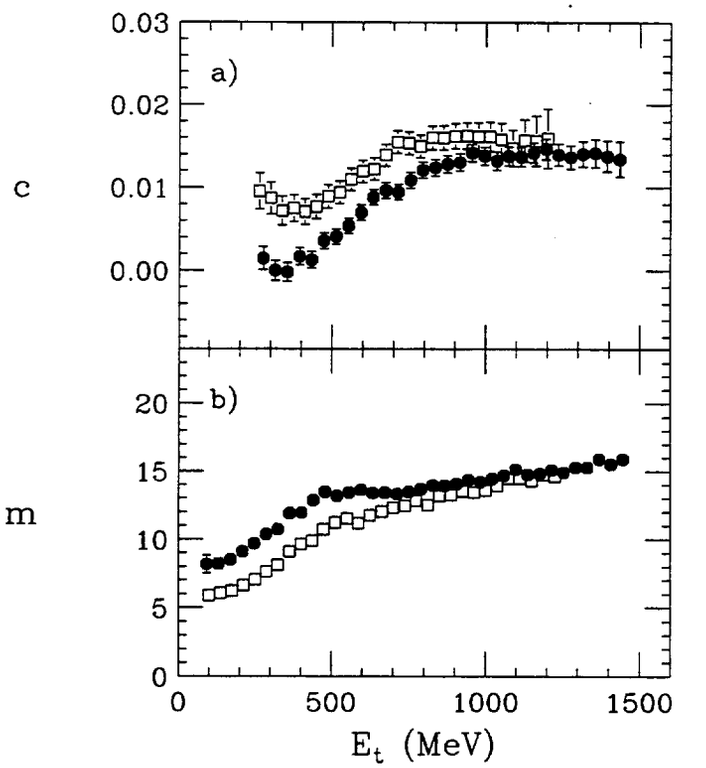

Fig. 11. From the experimental ^{129}Xe + ^{197}Au reaction at E/A = 50 MeV (squares) and 60 MeV (circles), as a function of E_t: a) Values of the quantity c, from the dependence of the charge distributions on the fold number n. b) Values of the binomial parameter m, from the mean and the variance of the IMF multiplicity distributions.

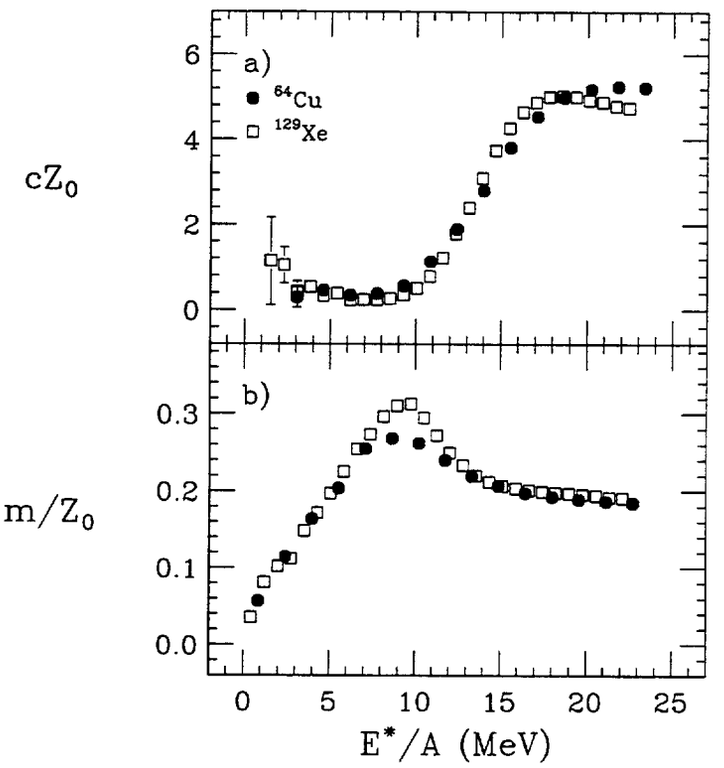

Fig. 12. Binomial decay of a ^{129}Xe source (squares) and a ^{64}Cu source (circles) with excitation energies and binomial parameters as in Fig. 10. Plotted as a function of the excitation energy per nucleon E^*/A: a) Values of cZ_o. b) Values of m/Z_o.

The small size effects on c are reminiscent of the small size effects on m, previously discussed in Sec. 2.3.4. As a consistency check of our simulation, one can compare the values of c and m from the ^{64}Cu source decay, presented in Figs. 10 and 8c, respectively. It is pleasing to observe that the deviation of c from zero, and the deviation of the extracted binomial parameter m from the input m_o/Z, occur simultaneously at the same excitation energy. Interestingly, a similar correlation between c and m has been observed also in some of the experimental data, as can be seen in Figs. 11a,b.

Worth noticing is also the scaling with the source size Z_o, that can be achieved, for both c and m, if one plots the quantities cZ_o and m/Z_o versus the excitation energy per nucleon, E*/A, as done in Figs. 12a,b. The scaling cZ_o is expected when breaking an integer into smaller integers in the least biased way (compare with the solution of Euler's problem, [23]). The scaling m/Z_o is also expected within a space-like scenario of multifragment decay, as already discussed in Sec. 2.3.2.

From these binomial simulations, we have achieved a better understanding of the physical meaning of the experimental quantities c and m. However, whether these quantities also bear a signature of dynamical processes occurring in multifragmentation, remains a fascinating question open for further investigations.

3 Transverse Energy, Poisson and Binomial Distributions

3.1 Transverse Energy

We shall now direct our attention towards technical issues raised by the use of the transverse energy, as an indicator of the system excitation energy, in the experimental studies of reducibility and thermal scaling [18,19,21].

We have seen that the Arrhenius plot establishes a relationship between the elementary single-fragment emission probability p and the temperature of the source. Therefore ideally one would like to verify reducibility at fixed values of the excitation energy. Experimentally, however, the temperature is determined indirectly by measuring the transverse energy E_t, a quantity related to the excitation energy [23]. Even though a linear correlation has been demonstrated between E^* (as determined from the kinematically-reconstructed source velocity) and E_t [23], the correlation is not sharp. Moreover, the measured transverse energy of an event is, by definition (see Eq. (1)), correlated with the number of IMFs detected in the event.

In this section we want to study whether the experimentally observed features of binomial reducibility and thermal scaling, based on the assumption that events selected at a given E_t arise mainly from one value of E^*, are affected by the width of the correlation between E_t and E^*, and by a possible auto-correlation between the measured transverse energy and the number of IMFs in an event.

3.2 Poisson Simulation

In order to investigate the event fluctuations associated with the use of the transverse energy, and in particular the conditions under which these fluctuations are sufficiently large to distort a Poisson distribution into a binomial distribution, we have performed simple Poisson simulations for intermediate mass fragment (IMF), light charged particle (LCP) and neutron (NEUT) multiplicities as a function of excitation energy, and then studied the resulting multiplicity distributions as a function of the transverse energy.

The Poisson simulation input values for $\langle N_{\rm IMF}\rangle\,(E^*)$ and $\langle N_{\rm LCP}\rangle\,(E^*)$ are taken from the experimental ^{129}Xe $+^{197}$ Au data at E/A = 60 MeV and are shown in Fig. 13a. As suggested by experimental investigations of the correlation between the transverse energy and the excitation energy [23], we assume $E^*{=}3E_t^{\rm exp}$, where $E_t^{\rm exp}$ is the experimentally measured transverse energy. The proportionality constant is 3 rather than 3/2 in order to account for the missing neutrons. For simplicity, the input $\langle N_{\rm NEUT}\rangle\,(E^*)$ is taken equal to $\langle N_{\rm LCP}\rangle\,(E^*)$, with the same excitation energy dependence. The resulting distributions in $\langle N_{\rm IMF}\rangle$, $\langle N_{\rm LCP}\rangle$ and $\langle N_{\rm NEUT}\rangle$ are completely

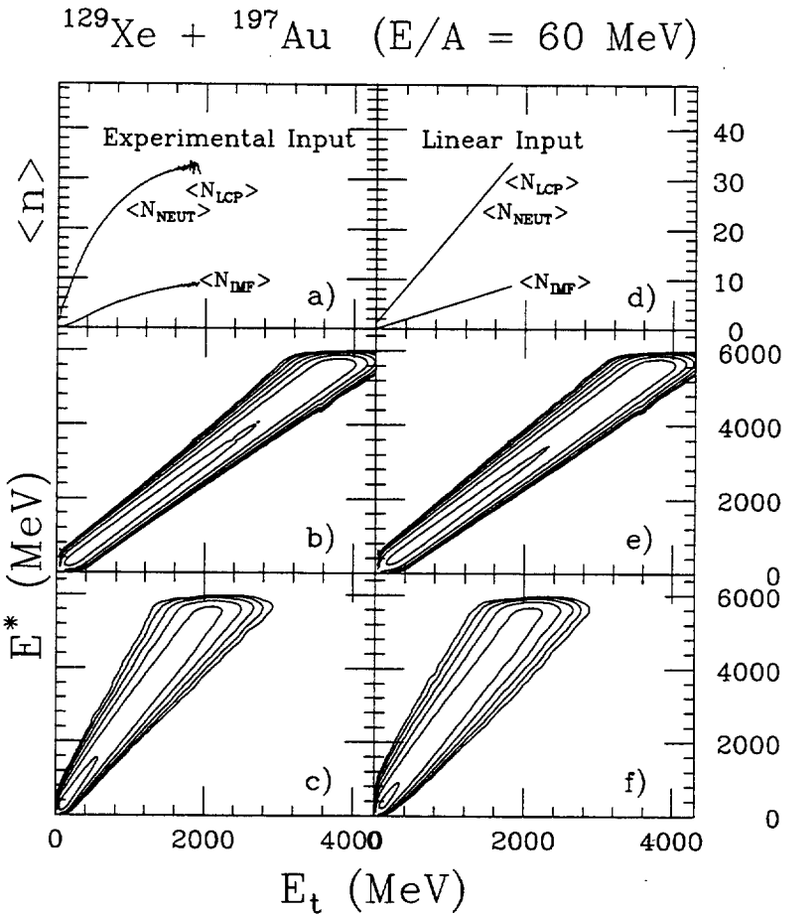

Fig. 13. a) Poisson simulation input values $\langle N_{\rm NEUT}\rangle$, $\langle N_{\rm LCP}\rangle$, $\langle N_{\rm IMF}\rangle$ as a function of E_t, taken from the ^{129}Xe + ^{197}Au reaction data at E/A = 60 MeV. b) Logarithmic contour plot of the correlation between E^* and E_t (calculated including neutrons) observed for the Poisson particle emission simulation. c) Correlation between E^* and E_t^m (calculated excluding neutrons). d) Linear input values $\langle N_{\rm NEUT}\rangle$, $\langle N_{\rm LCP}\rangle$, $\langle N_{\rm IMF}\rangle$ as a function of E_t. e) Correlation between E^* and E_t. f) Correlation between E^* and E_t^m.

independent, since no charge or mass conservation is applied. In fact, no charge or mass information is used, and the distributions are identical, except that they are generated from different mean values and labelled as IMF, LCP and NEUT respectively. The polar (θ) and the azimuthal (ϕ) angles of these emitted particles are distributed isotropically. The excitation energy is assumed thermal, and the kinetic energy of each particle is set equal to $E = E^*/N$ with $N = N_{\rm IMF} + N_{\rm LCP} + N_{\rm NEUT}$. For simplicity, no Coulomb trajectory calculation is implemented, and the transverse energy of each particle is calculated according to its definition, $E_t^i = E_i \sin^2\theta_i$.

3.2.1 E^*-E_t Correlation

The average transverse energy for events of a fixed excitation energy can be calculated as:

$$\langle E_t \rangle = \left\langle \sum_i^N \frac{E^*}{N} \sin^2\theta_i \right\rangle = E^* \frac{\int \sin^2\theta_i d\cos\theta_i}{\int d\cos\theta_i} = \frac{2}{3}E^*. \tag{14}$$

The above equation clearly shows that the average transverse energy of a class of events depends solely on the excitation energy, and is independent of the number of particles emitted. This implies that there is no correlation between the particle multiplicity n and the transverse energy of an event, other than their individual dependence on the excitation energy. In this context, n can be $N_{\rm IMF}$, $N_{\rm LCP}$ or $N_{\rm NEUT}$ for fragment, light charged particle and neutron multiplicity respectively.

The simulated correlation between E_t and E^* is plotted in Fig. 13b. A linear correlation is observed, and the value of $\langle E_t \rangle$ is $2/3E^*$, consistent with the prediction of Eq. (14). This shows that the events with a given E_t, come from a rather narrow distribution of E^* with centroid $= 3/2E_t$. Therefore, the resulting multiplicity distribution at a given transverse energy $P_{E_t}(n)$, is an average of multiplicity distributions $P_{E^*}(n)$ weighted by the excitation energy distribution at that transverse energy, $P_{E_t}(E^*)$:

$$P_{E_t}(n) = \int P_{E_t}(E^*) \cdot P_{E^*}(n) dE^*. \tag{15}$$

The question naturally arises whether this folding procedure introduces large event fluctuations. In particular, under what circumstances will the mean and variance information of $P_{E^*}(n)$ be preserved in the resulting multiplicity distribution $P_{E_t}(n)$? A trivial case is considered by assuming the multiplicity distribution $P_{E^*}(n)$ to be energy independent. The resulting multiplicity distribution from the above folding procedure (Eq. (15)) simply preserves the mean and variance information as shown below,

$$P_{E_t}(n) = \int P_{E_t}(E^*) \cdot P_{E^*}(n) dE^* = P(n) \int P_{E_t}(E^*) dE^* = P(n). \tag{16}$$

For more realistic situations, as in statistical decays, the particle emission probability increases with nuclear temperature, and thus introduces an energy dependence into the multiplicity distribution $P_{E^*}(n)$. In these cases, the fluctuations due to the spread in the excitation energy associated with events of a given transverse energy, can no longer be neglected. In fact, the resulting variance $(\sigma^2_{E_t})$ of $P_{E_t}(n)$ strongly depends on the variance $\sigma^2_{E^* E_t}$ of the excitation energy distribution $P_{E_t}(E^*)$.

When the correlation between E_t and E^* is strong, the distribution $P_{E_t}(E^*)$ becomes a δ function, and its corresponding variance $\sigma^2_{E^* E_t}$ approaches zero,

$$P_{E_t}(E^*) = \delta(E^* - \frac{3}{2}E_t). \tag{17}$$

In this limit, the resulting multiplicity distribution preserves the mean and variance information, namely:

$$\begin{aligned} P_{E_t}(n) &= P_{E^*=\frac{3}{2}E_t}(n) \\ \langle n \rangle_{E_t} &= \langle n \rangle_{E^*=\frac{3}{2}E_t} \\ \sigma^2_{E_t} &= \sigma^2_{E^*=\frac{3}{2}E_t}. \end{aligned} \tag{18}$$

However, when the correlation between E_t and E^* is weakened, the spread in the excitation energy at a given value of E_t becomes broader (i.e. $\sigma^2_{E^*E_t} > 0$). The multiplicity distribution $P_{E_t}(n)$ is now an average over events with a range of E^*, and this introduces event fluctuations. When the excitation energy distribution is symmetric with respect to $E^* = \frac{3}{2}E_t$, the information for the average multiplicity $\langle n \rangle$ is still preserved according to Eq. (18), but the corresponding variance is broadened by this folding procedure, namely,

$$\sigma^2_{E_t} > \sigma^2_{E^*=\frac{3}{2}E_t}. \tag{19}$$

As a result, the ratio $\sigma^2_{E_t}/\langle n \rangle_{E_t}$ becomes larger than the Poisson value of 1. This distortion of a Poisson distribution due to event fluctuations arising from the use of E_t does not lead to a binomial distribution, which is characterized by a ratio $\sigma^2_{E_t}/\langle n \rangle_{E_t}$ smaller than unity.

3.2.2 E_t Auto-Correlation

Recently Del Zoppo *et al.* [39] have claimed that the use of global observables, which exhibit event-to-event fluctuations, might introduce auto-correlations between pairs of observables that may "simulate specific signatures of a particular physical regime". In particular, since the measured transverse energy is such a global observable, correlated with the number of detected fragments of an event, it has been suggested [39,40] that the feature of binomial reducibility might arise from the correlation between the measured transverse energy and the number of detected fragments ($N_{\rm IMF}$).

In Ref. [39] it is empirically observed that the multiplicities $N_{\rm LCP}$ of light charged particles (LCP, $Z \leq 2$), emitted from the reaction ^{132}Xe + ^{158}Gd at a bombarding energy of E/A = 44 MeV, are binomially distributed at any given transverse energy. These distributions are assumed to be originally Poissonian, and the observed binomial nature is shown to arise from the auto-correlation between the measured transverse energy and the light charged particle multiplicity. As a point of fact, in the analysis of Ref. [39], only the very particles whose multiplicities are studied contribute to the measurement of the transverse energy, and the measured value of the transverse energy is therefore strongly dependent upon the number of detected particles. This auto-correlation leads to narrow distributions of $N_{\rm LCP}$ over the entire range of measured transverse energy. Consequently the variance becomes smaller than the mean $\langle N_{\rm LCP} \rangle$, and this deviation from the Poisson distribution grows with increasing auto-

correlation. Eventually the binomial approach becomes appropriate for describing the $N_{\rm LCP}$ distributions.

We now proceed to verify the effects of event-to-event fluctuations introduced by the transverse energy on the $N_{\rm IMF}$ and $N_{\rm LCP}$ distributions, within our Poisson simulations. In order to verify whether a Poisson distribution is distorted, we rely on several quantities that bear unique properties in the Poisson limit. First of all, the ratio $\sigma^2_{E_t}/\langle n\rangle_{E_t}$ and its deviation from the Poisson value of 1 is examined. Then we study the quantity $g(n)$ defined as follows [41]:

$$g(n) = \frac{(n+1)P(n+1)}{P(n)}, \tag{20}$$

where $P(n)$ is the probability to observe an event of particle multiplicity n. In the Poisson limit:

$$g(n)_{Poisson} = \frac{(n+1)\frac{<n>^{n+1}e^{-<n>}}{(n+1)!}}{\frac{<n>^{n}e^{-<n>}}{n!}} = \langle n\rangle\,, \tag{21}$$

$g(n)$ is independent of n. Therefore, the slope of $g(n)$ versus n is 0, and the corresponding y-intercept is equal to the average particle multiplicity $\langle n\rangle$.

In Fig. 14, we plot the ratio $\sigma^2/\langle n\rangle$ along with the slope and y-intercept of $g(n)$ versus n as a function of transverse energy, for both the $N_{\rm IMF}$ and $N_{\rm LCP}$ distributions. In both cases, the ratios $\sigma^2/\langle n\rangle$ scatter around the value of 1. The plots of $g(n)$ versus n are flat and their y-intercepts agree reasonably well with the solid lines corresponding to the average particle multiplicities $\langle n\rangle$. These observations indicate that the Poisson nature of the $N_{\rm IMF}$ and $N_{\rm LCP}$ distributions is preserved when one uses E_t as a measure of E^*. However, if we look at Fig. 14 more carefully, a small systematic discrepancy is observed between the slopes (symbols) of $g(n)$ versus n and the dashed lines at low E_t (Figs. 14c,d). The fact that the ratios $\sigma^2/\langle n\rangle$ are slightly larger than 1 in the same region (Figs. 14a,b), suggests that this small deviation from the Poisson limit is not caused by auto-correlation, but rather by the random event fluctuations as a result of the folding procedure described by Eq. (15).

The results of these Poisson simulations show that there is no auto-correlation between E_t and $N_{\rm IMF}$ or $N_{\rm LCP}$ under the assumption that the excitation energy is thermal and evenly distributed among the emitted particles. The event fluctuations associated with E_t will at most increase the ratio $\sigma^2/\langle n\rangle$ of the resulting multiplicity distribution $P_{E_t}(n)$. Hence, this distortion of a Poisson distribution does not lead to a binomial distribution.

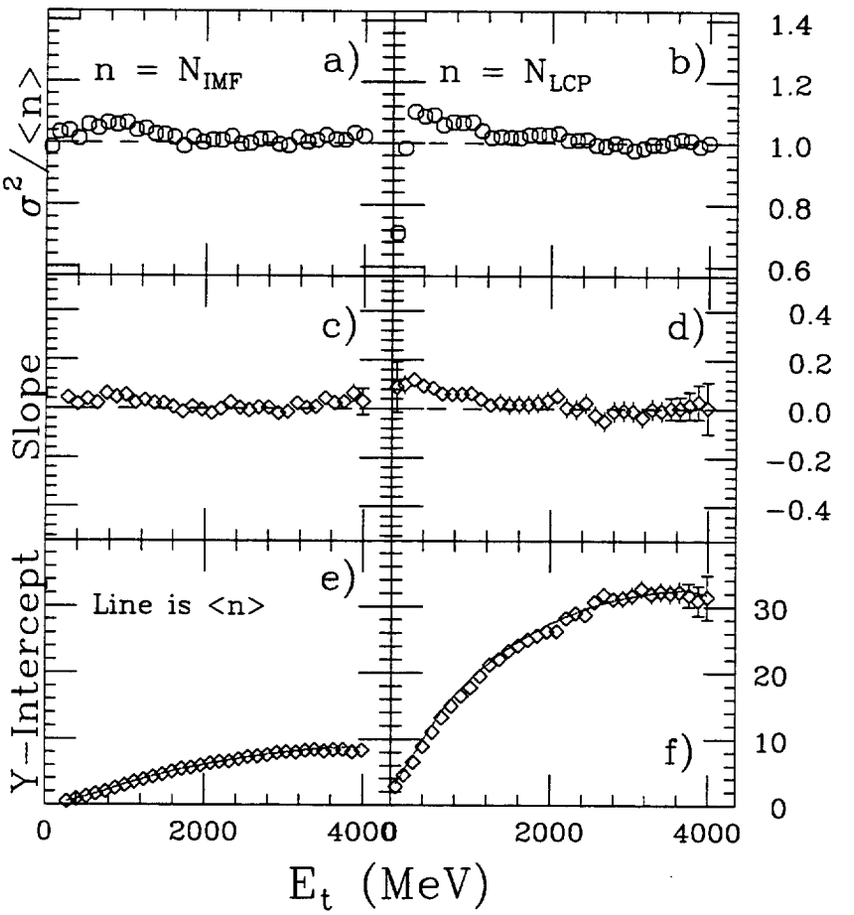

Fig. 14. For the N_{IMF} (left column), and N_{LCP} distributions (right column) generated from the Poisson simulation using the experimental input, plotted as a function of E_t: a), b): Ratio $\sigma^2/\langle n\rangle$. c), d): Slope of $g(n)$ vs n. e), f): y-intercept of $g(n)$ vs n. The solid lines in panels (e) and (f) indicate the values of $\langle N_{\mathrm{IMF}}\rangle$ and $\langle N_{\mathrm{LCP}}\rangle$ as a function of E_t.

3.2.3 E_t Auto-Correlation and Detection Efficiency

Thus far, we have assumed 100% efficiency to measure E_t. In actual experiments the detection system is not perfect, and the measured transverse energy E_t^m may be different from the true E_t. For instance, neutrons have not been detected in the experiments of Refs. [18,19] even though they carry kinetic energy and contribute significantly to the transverse energy of a given event. In this case, the transverse energy of a given event is underestimated ($E_t^m < E_t$).

In an attempt to study the effect of the missing neutrons in the measurement of the transverse energy, we have repeated the above analysis with E_t^m calculated from charged particles only. The simulated correlation between E_t^m and E^* is plotted in Fig. 13c, and can be compared with the correlation between E_t and E^* plotted in Fig. 13b. A linear correlation between $\langle E_t^m\rangle$ and E^* still exists, but the distribution at a given E_t^m becomes broader.

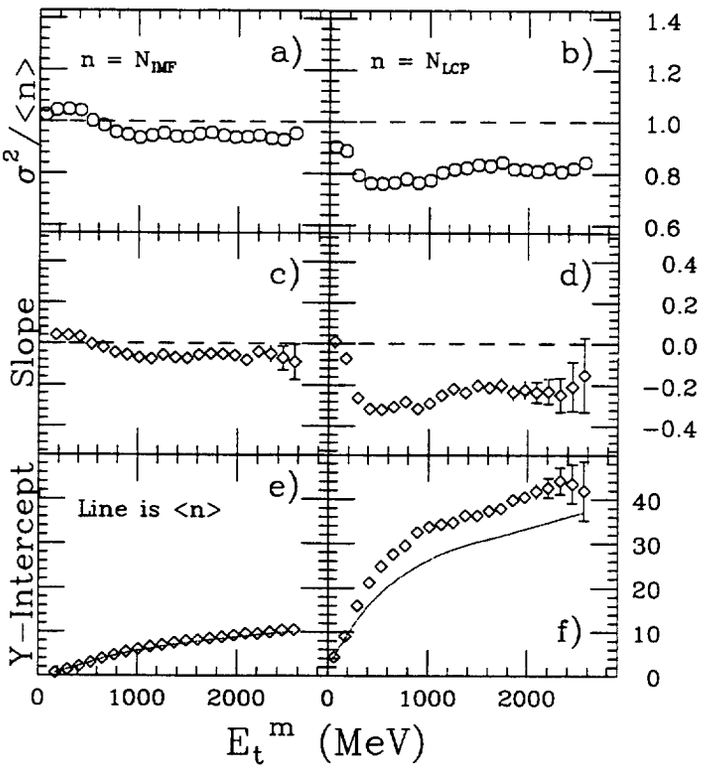

Fig. 15. For the N_{IMF} (left column), and N_{LCP} distributions (right column), generated from the Poisson simulation using the experimental input, plotted as a function of E_t^m: a), b): Ratio $\sigma^2/\langle n\rangle$. c), d): Slope of $g(n)$ vs n. e), f): y-intercept of $g(n)$ vs n. The solid lines in panels (e) and (f) indicate the values of $\langle N_{\mathrm{IMF}}\rangle$ and $\langle N_{\mathrm{LCP}}\rangle$ as a function of E_t^m.

In Fig. 15, we plot the ratio $\sigma^2/\langle n\rangle$ along with the slope and y-intercept of $g(n)$ versus n as a function of E_t^m, for both the N_{IMF} and N_{LCP} distributions obtained from the above Poisson simulations. For the N_{LCP} distribution (right column), the ratio $\sigma^2/\langle N_{\mathrm{LCP}}\rangle$ is scattering around a value of 0.8. The slope of $g(N_{\mathrm{LCP}})$ versus N_{LCP} is negative, and the y-intercept is larger than the mean multiplicity $\langle N_{\mathrm{IMF}}\rangle$ at all values of E_t^m. In other words, the Poisson nature of N_{LCP} is not preserved at all values of E_t^m. Since the value of the total charged particle multiplicity and thus of E_t^m arises mainly from LCPs, a strong auto-correlation between N_{LCP} and E_t^m is not unexpected. In this case, events with a given E_t^m arise from a very narrow distribution of N_{LCP}, and the distribution $P_{E_t}(n)$ does not follow the folding procedure of Eq. (15). Consequently, the variance becomes less than the mean, and the extraction of the binomial parameters p and m becomes feasible. These extracted quantities are plotted as a function of E_t^m in Fig. 16. The probabilities of emitting n light charged particles, are also plotted as a function of E_t^m using different symbols for N_{LCP} ranging from 3 to 30, together with the solid lines generated from the binomial calculations (Eq. (2)) using the above extracted values of p and m. Excellent agreement between the data (symbols) and the calculations (curves), for the entire range of E_t^m, confirms the binomial nature of the distorted distributions. Remarkably, the elementary probability p is nearly constant with E_t^m. This confirms the findings of [39].

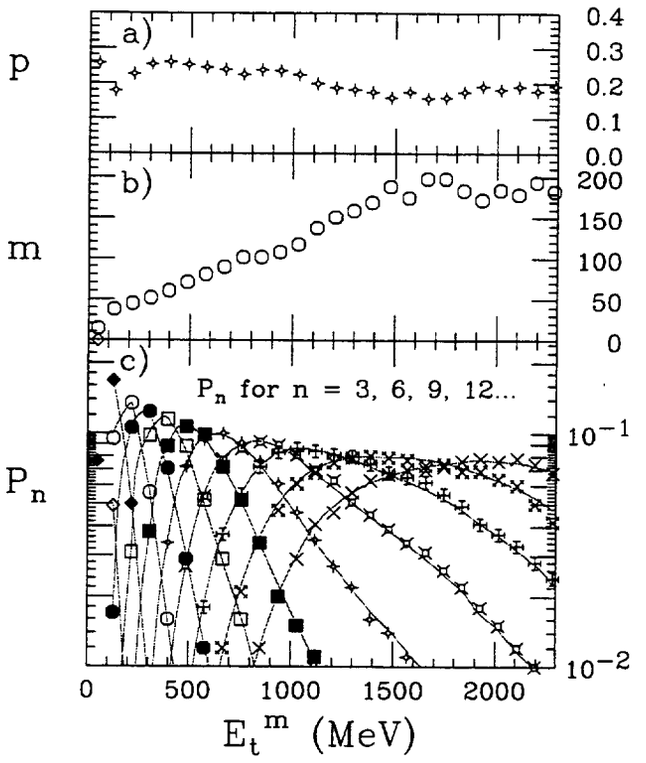

Fig. 16. For the N_{LCP} distribution generated from the Poisson simulation, plotted as a function of E_t^m: a) Values of p extracted from the mean and variance. b) Values of m extracted from the mean and variance. c) Probability to emit n light charged particles. The curves are binomial calculations.

On the other hand, IMFs contribute very little to the total multiplicity of charged particles, and thus to E_t^m, so the auto-correlation between E_t^m and N_{IMF} should be relatively weak, as shown in Fig. 15, left column. The y-intercept of the $g(N_{\mathrm{IMF}})$ versus N_{IMF} plot collapses onto the line corresponding to the mean fragment multiplicity $\langle N_{\mathrm{IMF}} \rangle$ at all values of E_t^m. A small negative slope is observed, and the ratio $\sigma^2 / \langle N_{\mathrm{IMF}} \rangle$ is slightly less than unity except at the region of low E_t^m, where the slope and the ratio $\sigma^2 / \langle N_{\mathrm{IMF}} \rangle$ are just larger than zero and unity respectively. This suggests that in the region of low E_t^m, the auto-correlation between N_{IMF} and E_t^m is negligible, and the residual event fluctuations slightly increase the variance of the N_{IMF} distributions. At higher E_t^m, the auto-correlation becomes observable, but the distortion of the Poisson nature is still very weak since the IMF contribution to E_t^m is only about 20% on average in this simulation.

Thus far, the Poisson simulation results are based on Poisson distributions generated from a specific set of inputs. These inputs (Fig. 13a) appear to be parabolic functions of E^*. In order to study the sensitivity of the multiplicity distributions to different inputs, and for the sake of comparison, we have performed Poisson simulations with a new set of inputs that are linear functions of E^*. More specifically, in Fig. 13d, the end points of the experimental inputs have been joined with straight lines to the origin, and used as linear inputs. The simulated correlations between the transverse energies

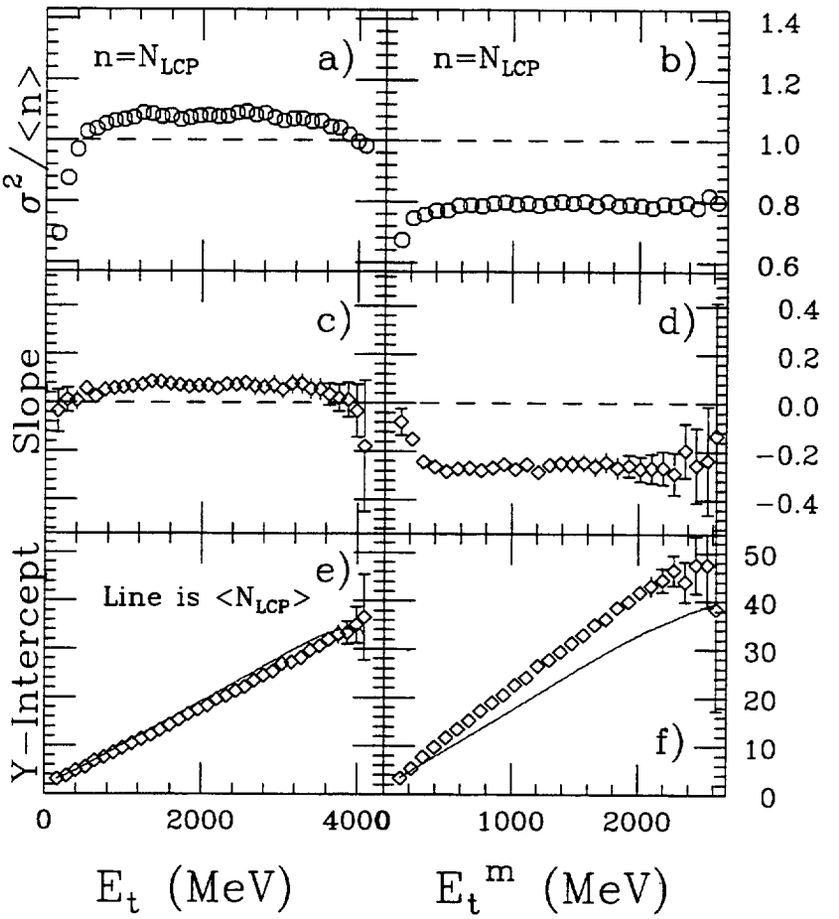

Fig. 17. For the N_{LCP} distribution generated from the Poisson simulation using the linear input, plotted as a function of E_t (left column) and E_t^m (right column): a), b): Ratio $\sigma^2/\langle n\rangle$. c), d): Slope of $g(n)$ vs n. e), f): y-intercept of $g(n)$ vs n. The solid lines in panels (e) and (f) indicate the values of $\langle N_{\mathrm{LCP}}\rangle$ as a function of E_t and E_t^m.

(E_t and E_t^m) and the excitation energy (E^*) are shown in panels (e) and (f) of Fig. 13. In both cases, the correlations are linear, consistent with the prediction of Eq. (14). We have also studied the effects of the fluctuations associated with E_t and E_t^m on the resulting N_{LCP} distribution, and the results shown in Fig. 17 are similar to those obtained for the experimental inputs. The event fluctuations associated with E_t clearly broaden the N_{LCP} distribution and thus increase the ratio $\sigma^2/\langle N_{\mathrm{LCP}}\rangle$ (Fig. 17a). On the other hand, the strong auto-correlation between E_t^m and N_{LCP} distorts the Poisson distribution in the opposite direction by decreasing the ratio $\sigma^2/\langle N_{\mathrm{LCP}}\rangle$ (Fig. 17b). Consequently, the relative magnitude of $\sigma^2/\langle N_{\mathrm{LCP}}\rangle$ can be used to distinguish the effect of random event fluctuations from that of auto-correlation.

The above study suggests that the transverse energy serves as a good observable for the measurement of the excitation energy. It has a rather sharp correlation with the excitation energy and has no auto-correlation with the fragment and light charged particle multiplicities being studied. On the other hand, if the measurement of the transverse energy is not perfect (possibly due to finite detection efficiency), an auto-

correlation between $N_{\rm LCP}$ and the measured transverse energy E_t^m may be introduced. The experimental setup of Del Zoppo *et al.* [39] does not measure neutrons, and the geometric acceptance for charged particles is rather limited due to the lack of forward angular coverage. As a result, the auto-correlation effect in their analysis is likely to be strong, and this is the reason for their observation of binomial distributions characterized by flat Arrhenius plots for the light charged particles. On the other hand, IMF yields contribute at most 20% on average to the measured transverse energy E_t^m in multifragmentation studies at intermediate energies. Therefore, the auto-correlation between $N_{\rm IMF}$ and E_t^m is not sufficient to distort a Poisson distribution into a binomial distribution.

The above discussion demonstrates that E_t can serve as a useful observable for the measurement of E^* in multifragmentation studies. In particular, the mean and variance of the N_{IMF} distribution are reasonably well preserved, even when the measurement of E_t is imperfect and limited by detection efficiency. This gives us confidence that the experimentally observed binomial fragment multiplicity distributions as a function of E_t have indeed their origin from parent binomial distributions.

3.3 Transverse Energy from Binomial Distributions

The correlation between E^* and E_t has been simulated also with the binomial event generator. We will present the results obtained from the binomial decay of a ^{197}Au source. The number of events simulated at each excitation energy step, has been established according to a monotonic relationship between the excitation energy and the collision impact parameter [42]. The transverse energy has then been calculated event-by-event from all emitted particles (E_t) and from charged particles only (E_t^m).

Fig. 18a is a logarithmic contour plot of the correlation between E^* and E_t. The correlation is rather narrow and the mean value of E_t at each E^* is a nearly straight line passing through zero, with proportionality constant approaching the expected value of $E_t = 2/3E^*$ (Eq. (14)). The correlation between E^* and E_t^m is shown in Fig. 18b. The linearity is preserved, although the proportionality constant between E^* and E_t^m is changed, and the distribution at a given E_t^m becomes broader. This is in agreement with the results of the Poisson simulations (compare with Fig. 13).

We now proceed by repeating the reducibility and thermal scaling analysis of the simulated events, as a function of the transverse energy. The values of $1/p$ are plotted as a function of $1/\sqrt{E_t}$ in Fig. 19a (squares), and can be compared with $1/p$ versus $1/\sqrt{E^*}$ in Fig. 19b (diamonds). Due to the linear correlation between E^* and E_t, the effect of using E_t instead of E^* to construct the Arrhenius plot is mainly a "stretching" of the x-axis (by a factor $\sqrt{3/2}$), even though a small distortion of the linearity of the plot is observed as well. If the x-axis of the Arrhenius plot is converted to the excitation energy scale with the linear relationship $E_t = 2/3E^*$ (squares in Fig.

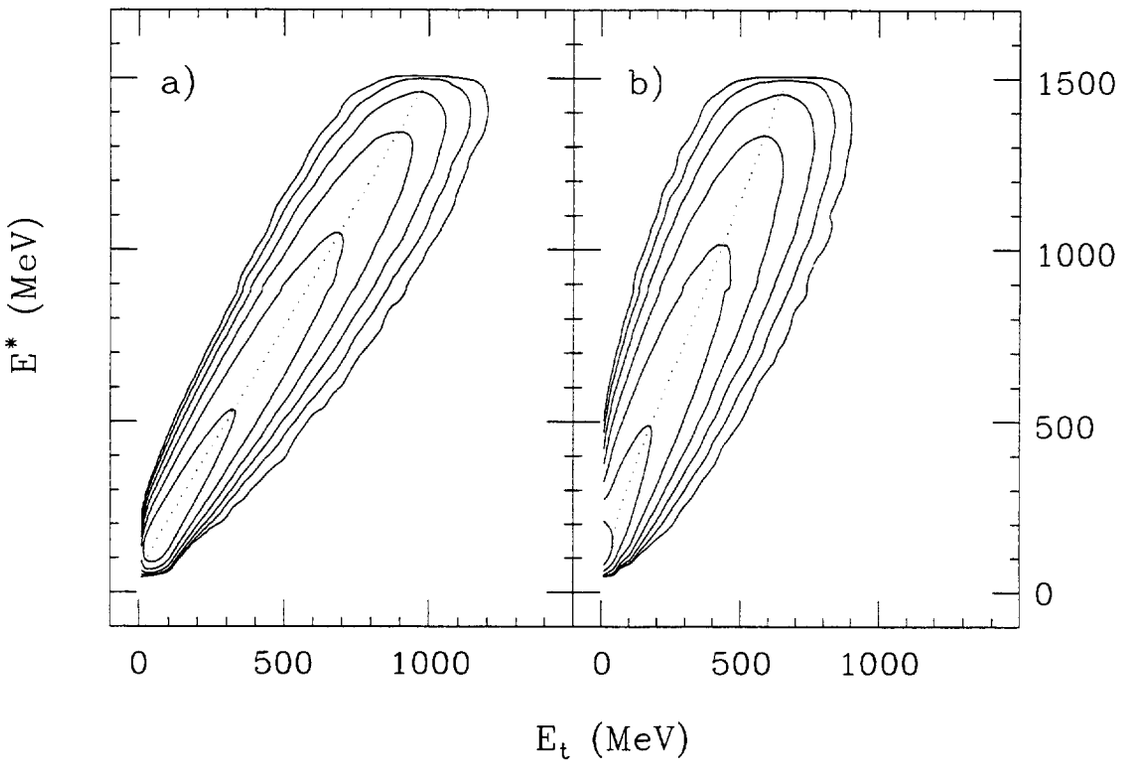

Fig. 18. Logarithmic contour plots of the correlation between E^* and E_t, calculated from the binomial decay of a ^{197}Au source with excitation energies in the range of 100 to 1500 MeV and binomial parameters $m_o(E^*) = 0.03 \cdot E^*$, $B_Z = (3 \cdot Z)$ MeV. a) E_t calculated from all particles including neutrons. b) E_t^m calculated from charged particles only. Dotted lines: mean value of E^* as a function of E_t.

19b), one observes nearly the same slope as the input to the calculation (diamonds), with differences of about 10%. A similar result is obtained when E_t^m (calculated from charged particles only) is utilized (circles of Fig. 19). The correct slope of the Arrhenius plot is recovered by rescaling the x-axis with the relationship between E^* and E_t^m (plotted as dotted line in Fig. 18b).

The accuracy of the barrier extraction, from the slopes of the rescaled E_t-Arrhenius plots, shows that events with a given E_t come from a rather narrow distribution of E^*, and that IMFs do not contribute significantly to the running variable E_t in the binomial simulations. In fact, for a typical ^{197}Au source decay, in the excitation energy range of 500 to 1000 MeV, about 40% of E_t is contributed by neutrons, 50% by light charged particles and only 10% by IMFs. The IMFs' contribution drops to less than 5% at excitation energies below 250 MeV and rises to 20% at excitation energies larger than 1250 MeV. The barrier extracted from the slopes of the rescaled E_t-Arrhenius plots, gets even closer to the simulation input value if the reducibility analysis is performed with higher values of $Z_{\rm th}$ in the IMF definition. For $7 \leq Z_{\rm IMF} \leq 20$, the value of the input barrier is recovered, from the slope of the E_t-Arrhenius plot, to within 2% of the input value.

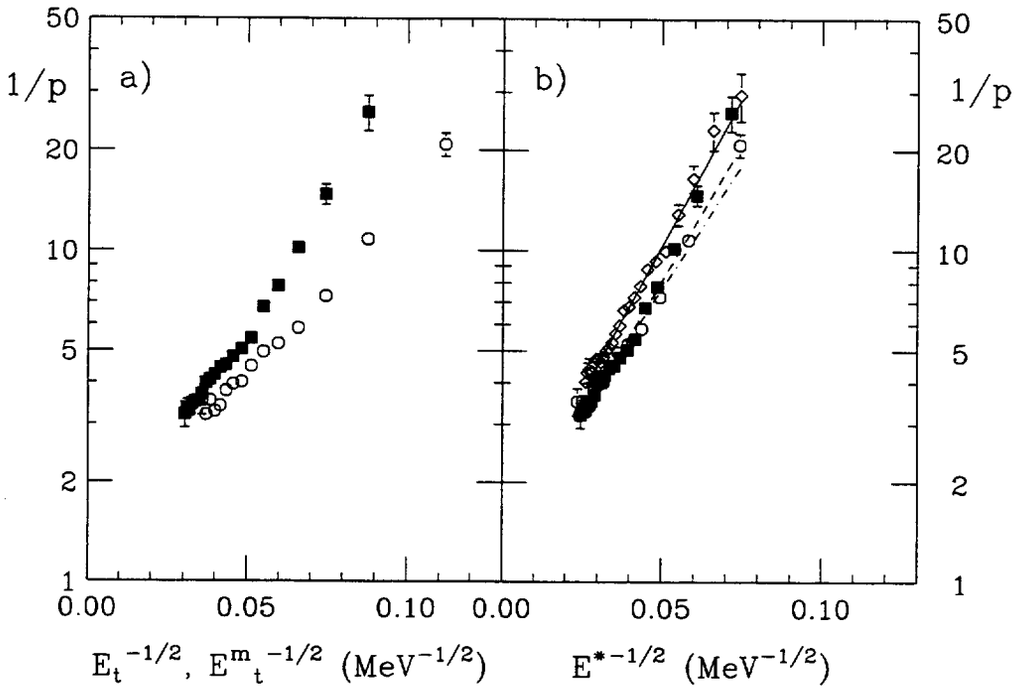

Fig. 19. Arrhenius plots from the binomial decay of a ^{197}Au source with excitation energies and binomial parameters as in Fig. 18. a) Squares: E_t-Arrhenius plot. Circles: E_t^m-Arrhenius plot. b) Diamonds: E^*-Arrhenius plot. Squares: rescaled E_t-Arrhenius plot. Circles: rescaled E_t^m-Arrhenius plot. Lines: straight line fits to the plots.

In conclusion, the binomial simulation results seem to suggest that the transverse energy, weakly correlated with the IMF multiplicities, linearly and strongly correlated with the system excitation energy, is a reliable observable for the analysis of reducibility and thermal scaling in multifragmentation.

4 Efficiency Effects

In this section we want to explore the effects of a finite detection efficiency on the extraction of the binomial parameter m and of the single fragment emission probability p. In particular, we want to investigate whether the Arrhenius plot is affected by incomplete detection coverage and reduced geometric efficiency, and whether there are effects, associated with the particular experimental devices used to collect the data, that may bias the experimental findings of binomial reducibility and thermal scaling.

After a general discussion on how the results from a binomial decay (and in particular the Arrhenius plot) are expected to be affected by a reduced detection acceptance (Sec. 4.1), we shall proceed by studying the effects of the specific experimental devices used to collect the data presented in Refs. [18,19,21] (Sec. 4.2).

4.1 Geometric Efficiency. E^*- and E_t-Arrhenius Plots

The reducibility of the n-fold probability to the 1-fold through the binomial equation introduces a great simplification in efficiency corrections. In fact, if the physical distribution is binomial, efficiency effects can be accounted for by correcting the binomial parameters p and m [18]. Disregarding details associated with anisotropies, multiple hits, energy thresholds etc., the true binomial probability p is expected to be related to the observed probability $p_{\rm obs}$ by the relationship:

$$p_{\rm obs} = p \cdot \epsilon \tag{22}$$

where ϵ is the geometric efficiency. The number of trials m is independent of the geometric efficiency.

The consequences of a reduced geometric acceptance on the Arrhenius plot are straightforward. Since

$$\ln \frac{1}{p_{\rm obs}} = \ln \frac{1}{p \cdot \epsilon} = \ln \frac{1}{p} + \ln \frac{1}{\epsilon} \tag{23}$$

one expects the Arrhenius plot to remain linear and conserve its slope, but to shift upwards by $\ln(1/\epsilon)$. In other words, the extracted barrier for single fragment emission is unchanged by a reduced geometric detection efficiency, while the absolute probability $p_{\rm obs}$ is trivially modified.

In order to test these ideas and investigate the effects of a finite acceptance on the experimental observables, angular cuts have been applied when counting the number of particles in a simulated binomial decay. The resulting Arrhenius plots and the values of the parameter m are presented in Fig. 20. As anticipated by Eq. (23), Fig. 20a shows that the effect of a reduced geometric efficiency on the E^*-Arrhenius plot is a shift of the intercept upwards, preserving the linearity and the slope of the plot, together with the physical information on the fragment emission barrier. For a given value of the geometric efficiency ϵ, the intercept of the Arrhenius plot is shifted by $\ln(1/\epsilon)$, according to Eqs. (22, 23). Fig. 20b shows that the extracted values of m are not affected by a reduced geometric acceptance.

Experimentally the Arrhenius plot is constructed using E_t as an estimate of the system excitation energy. The effects of a reduced geometric efficiency, when the transverse energy is involved, are somewhat more complicated since, by definition (Eq. (1)), the measured value of the transverse energy is correlated with the number of detected fragments. Fig. 21a shows the E_t-Arrhenius plots produced when angular cuts are applied in the binomial decay simulation, reducing the number of detected particles as well as the measured E_t. One can notice both a shift and a small change in the slope of the straight lines.

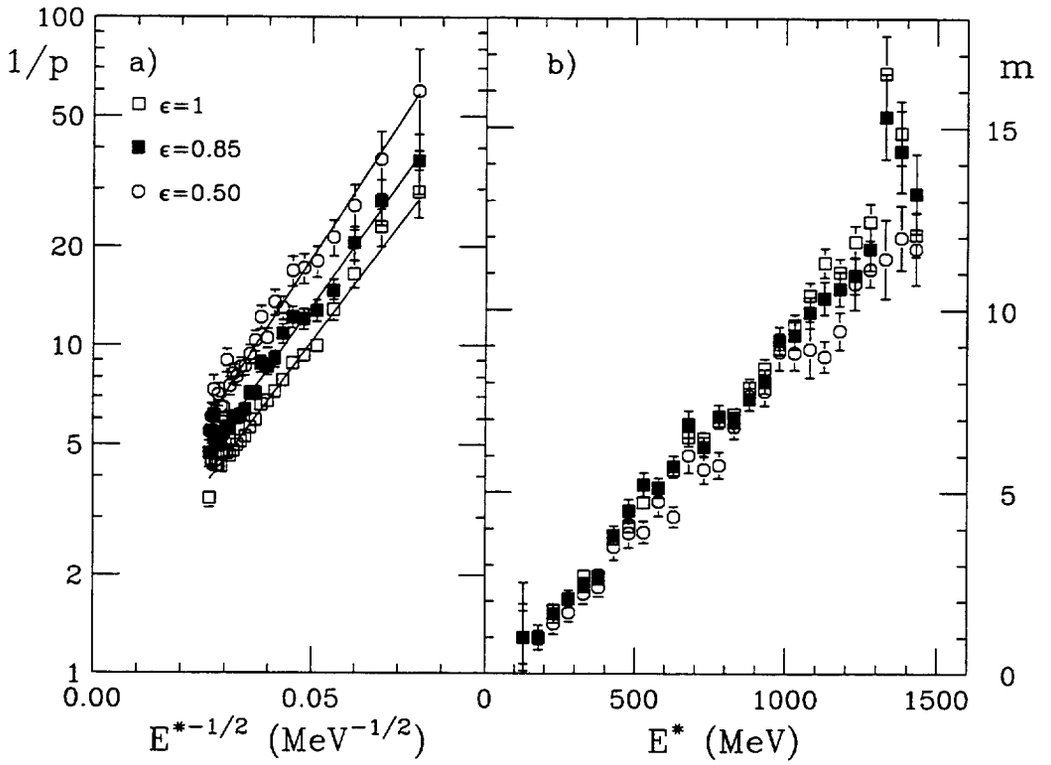

Fig. 20. Binomial decay of a ^{197}Au source with excitation energies and binomial parameters as in Fig. 18. Polar angle cuts (45°, 90°) are applied. a) E^*-Arrhenius plots (symbols) and straight line fits to the plots (solid lines). b) Extracted values of the binomial parameter m.

The experimental observation of a linear correlation between the upper limit of the measured transverse energy (E_t^{max}) and the available center of mass energy [29], has suggested the following rescaling procedure for the efficiency dependent E_t-Arrhenius plots. For each angular cut, corresponding to a certain geometric efficiency (ϵ), the upper limit of the transverse energy $E_t^{max}(\epsilon)$ is deduced at the tail of the corresponding transverse energy distribution (Fig. 21c), after cutting 0.1% of the total integrated yield. The values of $E_t^{max}(\epsilon)$ are plotted in Fig. 21d, normalized to $E_t^{max}(\epsilon = 1)$ measured without angular cuts. The x-axis of the E_t-Arrhenius plots of Fig. 21a, is now rescaled, multiplying $E_t(\epsilon)$ by the ratio $E_t^{max}(\epsilon = 1)/E_t^{max}(\epsilon)$. The rescaled Arrhenius plots collapse nicely on top of each other, as shown in Fig. 21b. The value of the simulation input barrier can finally be extracted from their common slope, if the relationship $E^* = 3/2E_t$ is taken into account.

A similar investigation of the efficiency effects on the Arrhenius plots has been performed with the experimental data of Ref. [19]. The detection efficiency has been artificially reduced by blocking, in software, some of the detectors according to their azimuthal angles. The results are qualitatively consistent with the simulation, strengthening our confidence in the reducibility approach and in the interpretation of the binomial parameters p and m. However, the extraction of the actual value of the barrier from the experimental data has not been possible, since the experimental relationship between the system excitation energy and the measured transverse energy

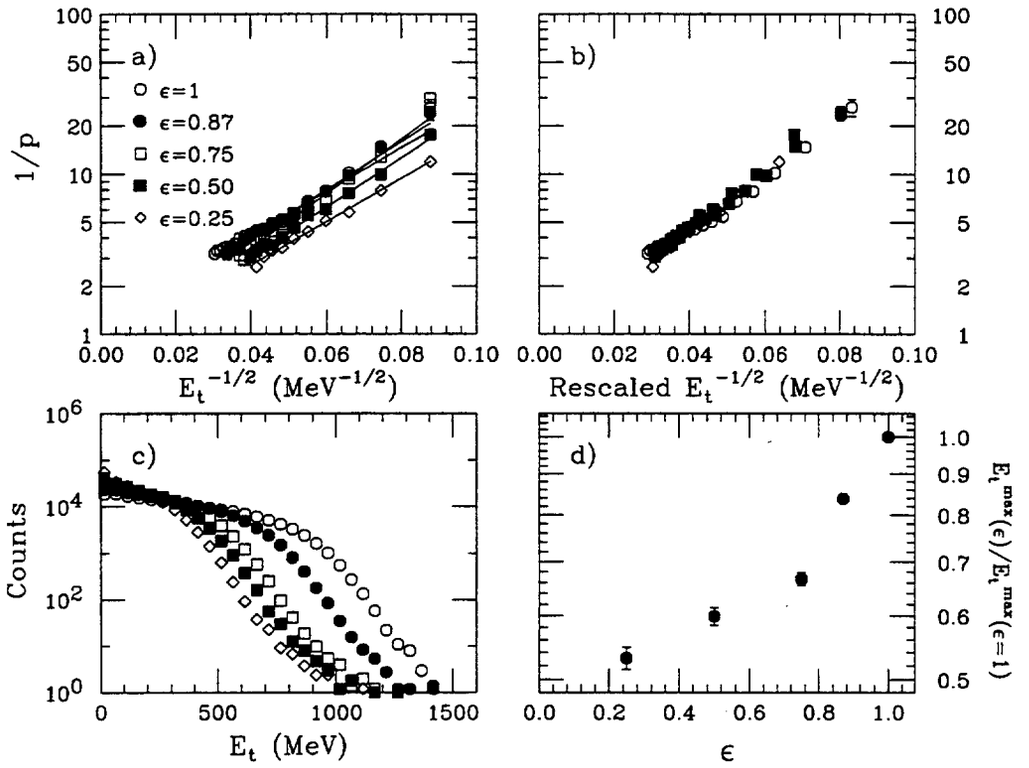

Fig. 21. Binomial decay of a ^{197}Au source with excitation energies and binomial parameters as in Fig. 18. Azimuthal angle cuts (45°, 90°, 180°, 270°) are applied, reducing the number of fragments and the measured transverse energy of the events. a) E_t-Arrhenius plots. b) Plots of panel (a) rescaled as explained in the text. c) E_t spectra. d) Dependence of E_t^{max} on the geometric efficiency.

is not known.

4.2 Filter Response

The experimental data presented in Ref. [19] were collected with a multidetector system covering 89% of 4π, consisting of the MSU Miniball (MB) array [43] and the LBL forward array [44]. Charged particles ($Z = 1 - 20$) emitted in the angular range 16°-160° were detected by 171 fast phoswich MB detectors. Charged particles (Z=1-54) emitted at forward angles (2°-16°) were detected by 16 Si-Si-plastic telescopes of the LBL array. The data of Refs. [18,21] instead were detected with the Miniball only, covering polar angles ranging from 9° to 160°. Representative detection thresholds for the MB and LBL arrays were: 2, 3, 4 MeV/A for Z=3,10,18 and 6, 13, 21, 27 MeV/A for Z=2, 8, 20, 54 respectively. The detector system was transparent to neutrons.

In order to simulate the complete MB-LBL array response, the fragments generated from the binomial simulation have been filtered through a software replica of the MB-LBL detection system. Since the simulated particles are emitted in the rest frame of the source, a source velocity has been added in order to perform a transformation

to the laboratory frame. After determining which detector (if any) is struck by each of the particles, the filter checks for energy thresholds and double hits. Therefore contributions to inefficiency can originate from geometric misses (either down the beam pipe at polar angles $< 2^{\circ}$ or in the dead regions between detectors), low energy particles stopped below the detection energy thresholds, and pairs of particles hitting simultaneously the same detector.

Simulations have been performed for the decay of a ^{197}Au source (with input parameters $B_Z = (3 \cdot Z)$ MeV, $m_o(E^*) = 0.03 \cdot E^*$, $100 \leq E^* \leq 1500$ MeV) varying the source velocity. The results show that the total efficiency for charged particles depends on the source velocity. A small source velocity causes a slight focusing of the events towards the forward LBL array. This increases the losses due to energy thresholds, since the LBL array thresholds are higher than those of the Miniball. A high source velocity minimizes the energy thresholds problem, but increases geometric losses in the beam pipe (as high as 35% of the total IMF yield), due to the stronger forward focusing. The detection efficiency is also dependent on the multiplicity of the events because of the increased probability of double hits in the same detector for high multiplicity events, and on the kinetic energies of the particles, through the detection energy thresholds. For these reasons the simulated detection efficiency is dependent on the excitation energy.

The filtered fold probabilities are still binomial and can be analyzed with the standard procedures. In Fig. 22 we show two examples of filtered E^*-Arrhenius plots. In one case (Fig. 22, solid squares, dashed line) a small source velocity increasing linearly with the temperature has been added to the particles from the ^{197}Au source decay. When comparing the filtered E^*-Arrhenius plot to the input Arrhenius plot (Fig. 22, diamonds, solid line), one can notice both a shift upwards, as expected when the geometric efficiency is reduced (Eq. (23)), and a slight tilt softening the slope of the line. This tilt originates from the dependence of the efficiency on the excitation energy as discussed above. In this simulation, the total detection efficiency for IMFs, integrated over the excitation energy, is $\approx 75\%$ (10% lower than the efficiency for light charged particles). The input barrier is recovered from the slope of the Arrhenius plot with an uncertainty of 15%.

In the other example of Fig. 22a (open circles, dash-dotted line), the source velocity is higher and decreasing linearly with the nuclear temperature. In this simulation, the total IMF efficiency drops to about 65%, due to higher losses of fragments kinematically focused at forward angles, beyond the geometric acceptance. However, the high source velocity minimizes the energy threshold effects and the resulting detection efficiency is rather constant over the entire range of excitation energies. The input slope is recovered with higher accuracy than in the previous case.

So far we have investigated the effects of the experimental filter on the E^*-Arrhenius plots. However, experimentally, we measure E_t-Arrhenius plots. Our simulations show that the filter causes a weakening of the correlation between the transverse energy

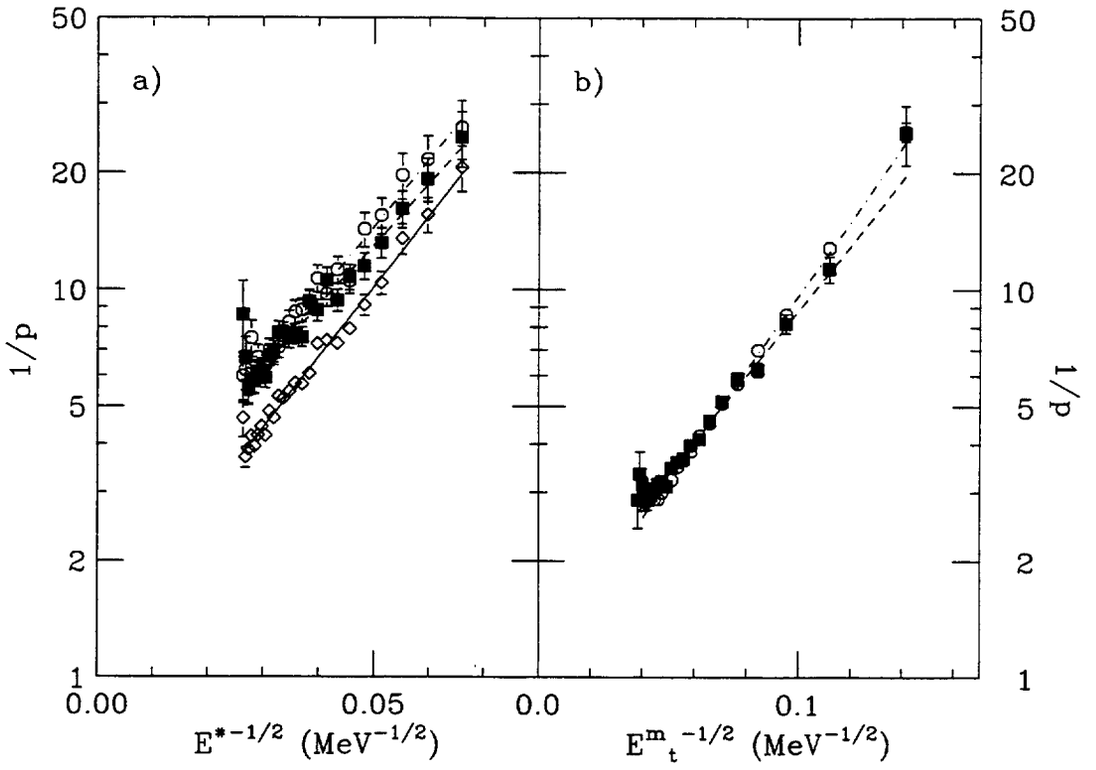

Fig. 22. Binomial decay of a ^{197}Au source with excitation energies and binomial parameters as in Fig. 18. a) Diamonds: input E^*-Arrhenius plot. Squares: filtered E^*-Arrhenius plot (v_{source} = 0 to 0.07 c). Circles: filtered E^*-Arrhenius plot (v_{source} = 0.2 c to 0.35 c). b) Squares: filtered E_t-Arrhenius plot (v_{source} = 0 to 0.07 c). Circles: filtered E_t-Arrhenius plot (v_{source} = 0.2 c to 0.35 c). All the lines are straight line fits to the plots.

and the excitation energy, due to a mixing of events from different excitation energies corresponding to the same measured value of E_t. When the filtered E_t is used for the Arrhenius plots, the barrier extracted from the slope has large uncertainties. However, it is still possible to extract values proportional to the barrier, by increasing the lower Z_{th} threshold in the IMF definition (as discussed in Sec. 3.3). Fig. 22b presents the E_t-Arrhenius plots obtained from the analysis of the filtered n-fold IMF emission probabilities, for the two simulations discussed above. One can notice that when the filtered E_t is used to produce Arrhenius plots, the extrapolated y-axis intercept corresponds to values of p larger than one. A similar behavior, observed in the experimental Arrhenius plots (see for example Fig. 1d), had for long puzzled us, since one would expect the elementary probability p to approach unity in the limit of infinite temperature.

In conclusion, the experimental filter introduces an excitation energy dependence of the detection efficiency, plus a broadening of the correlation between E_t and E^*. The filtered Arrhenius plots are still linear, but their "true" slope, originating from the emission barrier, is generally not recoverable.

5 Summary

We have implemented binomial and Poisson decay simulations to address a number of issues connected to the experimental multifragmentation studies presented in Refs. [18,19,21–24]. For the binomial simulation, we have assumed that the n-fragment emission probabilities P_n are distributed according to the binomial distribution, and that multifragmentation is empirically reducible to a combination of nearly independent fragment emissions. Moreover, we have assumed a thermal dependence of the elementary emission probability p on the nuclear temperature.

By processing simulated events, we have tested the standard procedures utilized in the experimental data analysis. We have verified that the simulation input is recovered without significant loss of information and how the final results reflect different input conditions.

The simulation results strengthen the validity of the reducibility approach used in the experimental work and the physical meaning of quantities such as the elementary probability p. Reducibility is a valid approach also when multiple sources of fragment emission are created in the collision, if one of the sources is dominant. The Arrhenius plot is a powerful tool to explore the thermal features of the elementary probability p, even though the determination of the actual fragment emission barrier B, proportional to the slope of the plot, can be hampered by the presence of source residues and by small size effects.

From both binomial and Poisson simulations it appears that the total transverse kinetic energy E_t is a good observable that can be reliably used for the measurement of the excitation energy in multifragmentation studies at intermediate energies. In our simulations, the transverse energy is linearly correlated with the system excitation energy and weakly correlated with the IMF multiplicity. We have demonstrated that neither event-to-event fluctuations nor E_t auto-correlation effects are large enough to distort a Poisson distribution into a binomial distribution. In particular the mean and variance of the N_{IMF} distribution are reasonably well preserved, even when the measurement of E_t is limited by the detection efficiency.

We have tested the effects of a reduced geometric efficiency as well as the effects of a software replica of the detection device. We have shown that a reduced geometric efficiency preserves binomiality and that efficiency corrections can be applied through the binomial parameters p and m. We have explored the effects of a finite detection acceptance on the Arrhenius plot and have shown that when the geometric acceptance is reduced, it is still possible to recover the binomial input without significant loss of information. The introduction of an energy dependent efficiency, instead, can compromise this possibility, especially when the transverse energy is used as a measure of the system excitation energy.

Finally, we have also shown that, in a binomial decay scenario, the n-fold IMF charge

distributions are reducible to the 1-fold, consistent with the experimental findings. In the binomial simulation, the n-fold charge distributions are independent of the fold number n as long as a sizeable remnant serves as a reservoir of mass, charge and excitation energy. A dependence on n arises when the entire system is consumed.

In conclusion, the results of the decay simulations have made us more confident that the experimental procedures utilized in the data analysis of Refs. [18,19,21–24] are correct, and that the empirical findings of reducibility and thermal scaling in multifragmentation are not an artifact of incomplete detection efficiency nor are they generated by the auto-correlation of the variable used to estimate the excitation energy.

Acknowledgements

This work was supported by the Director, Office of Energy Research, Office of High Energy and Nuclear Physics, Nuclear Physics Division of the US Department of Energy, under contract DE-AC03-76SF00098.

References

[1] L.G. Moretto and G.J. Wozniak, *Ann. Rev. of Nucl. Part. Sci.*, **43** (1993) 379, and references therein.

[2] J.P. Bondorf *et al.*, *Phys. Reports* **257** (1995) 133, and references therein.

[3] D.H.E. Gross, *Nucl. Phys.* **A553** (1993) 175, and references therein.

[4] L.G. Sobotka *et al.*, *Phys. Rev. Lett.* **51** (1983) 2187.

[5] L.G. Moretto and G.J. Wozniak, *Prog. Part. Nucl. Phys.* **21** (1988) 401.

[6] J. Randrup and S.F. Koonin, *Nucl. Phys.* **A356** (1981) 223.

[7] G. Fai and J. Randrup, *Nucl. Phys.* **A404** (1983) 551.

[8] J.P. Bondorf *et al.*, *Nucl. Phys.* **A443** (1985) 321.

[9] D.H.E. Gross, *Rep. Prog. Phys.* **53** (1990) 605.

[10] W. Cassing and U. Mosel, *Prog. Part. Nucl. Phys.* **25** (1988) 235.

[11] X. Campi, *Phys. Lett.* B **208** (1988) 351.

[12] G.F. Bertsch and S. Das Gupta, *Phys. Rep.* **160** (1988) 190.

[13] J. Aichelin, *Phys. Rep.* **202** (1991) 233.

[14] C. Grégoire *et al.*, *Nucl. Phys.* **A465** (1987) 315.

[15] A. Bonasera *et al.*, *Phys. Lett.* B **221** (1989) 233, **246** (1990) 337, **361** (1995) 25.

[16] L.G. Moretto *et al.*, *Phys. Rev.* **179** (1969) 1176.

[17] L.G. Moretto *et al.*, *Phys. Rev. Lett.* **71** (1993) 3935.

[18] L.G. Moretto *et al.*, *Phys. Rev. Lett.* **74** (1995) 1530.

[19] K. Tso *et al.*, *Phys. Lett.* B **361** (1995) 25.

[20] L. Phair *et al.*, *Nucl. Phys.* **A548** (1992) 489.

[21] L. Phair *et al.*, *Phys. Rev. Lett.* **75** (1995) 213.

[22] L. Phair *et al.*, *Phys. Rev. Lett.* **77** (1996) 822.

[23] L.G. Moretto *et al.*, *Phys. Reports* (1996), accepted, LBNL-39388.

[24] A. Ferrero *et al.*, *Phys. Rev.* C **53** (1996) R5.

[25] A.S. Botvina and D.H.E. Gross, *Phys. Lett.* B **344** (1995) 6.

[26] L.G. Moretto *et al.*, *LBL Annual Report* LBL-35768 (1993) 89.

[27] R.J. Charity *et al.*, *Nucl. Phys.* **A476** (1988) 516.

[28] W.D. Myers, *Nucl. Phys.* **A204** (1973) 465.

[29] K. Tso, *Ph. D. Thesis*, LBNL-38884,
University of California at Berkeley (1996).

[30] W.A. Friedman, *Phys. Rev.* C **42** (1990) 667.

[31] W.A. Friedman, private communication.

[32] D.R. Bowman *et al.*, *Phys. Rev. Lett.* **70** (1993) 3534.

[33] C.P. Montoya *et al.*, *Phys. Rev. Lett.* **73** (1994) 3070.

[34] B. Lott *et al.*, *Phys. Rev. Lett.* **68** (1992) 3141.

[35] J. Toke *et al.*, *Phys. Rev. Lett.* **75** (1995) 2920, *Nucl.. Phys.* **A583** (1995) c519.

[36] J.F. Lecolley *et al.*, *Phys. Lett.* B **325** (1994) 317, *Phys. Lett.* B **354** (1995) 202.

[37] J. Lukasik *et al.*, IPNO-DRE-96-04, *Proceedings of the XXXIV Int. Winter Meeting on Nucl. Phys.*, Bormio (Italy), 22-27.

[38] L.G. Moretto *et al.*, *Phys. Rev. Lett.* **76** (1996) 372.

[39] A. Del Zoppo *et al.*, *Phys. Rev. Lett.* **75** (1995) 2288.

[40] W. Skulski *et al.*, *Nucl. Chem. Prog. Rep.* DOE/ER/40414-8, p. 75
University of Rochester (1995).

[41] A. Giovannini and L. Van Hove, *Z. Phys.* **C30** (1986) 391.

[42] C. Cavata *et al.*, *Phys. Rev.* C **24** (1990) 1760.

[43] R.T. De Souza *et al.*, *Nucl. Inst. Meth.* **A295** (1990) 109.

[44] W.L. Kehoe *et al.*, *Nucl. Inst. Meth.* **A311** (1992) 258.